Waveguide Simualtion Using Mode Matching Method

WAVEGUIDE SIMUALTION USING MODE MATCHING METHOD

BY

JUNFENG LI, B.Sc.

A THESIS

SUBMITTED TO THE DEPARTMENT OF ELECTRICAL & COMPUTER ENGINEERING

AND THE SCHOOL OF GRADUATE STUDIES

OF MCMASTER UNIVERSITY

IN PARTIAL FULFILMENT OF THE REQUIREMENTS

FOR THE DEGREE OF

MASTER OF APPLIED SCIENCE

Master of Applied Science (2014)   McMaster University

(Electrical & Computer Engineering)   Hamilton, Ontario, Canada

TITLE: Waveguide Simualtion Using Mode Matching Method

AUTHOR: Junfeng Li

                         B.Sc. (Applied Physics)

                         University of Science and Technology of China (USTC)

                         Hefei, China

SUPERVISOR: Dr. Wei-Ping Huang

                         Dr. Xun Li

NUMBER OF PAGES: xiv, 79

Abstract

Finite-Difference (FD) based complex modes solver and Complex Mode Matching Method (CMMM) is one of the most popular combinations in modeling and simulation of optical waveguides. This thesis covers the basic theories behind the approaches and important implementation details. Weighted Optical Path Distance is proposed to speed up convergence and improve numerical accuracy to deal with asymmetric structures. An improved formula is derived for Complex Mode Matching Method expansion process based on matrix optimization. The latter part applies the above approach in the modeling of bending structures and grating structures. Typical structures, including bending structures, straight-bend-straight structures, long-period gratings, gratings with deposited layer, gratings with deep corrugations, are investigated and analyzed.

Acknowledgements

I would like to express my sincere gratitude to Dr. W.P. Huang for giving me the opportunity to pursue further studies in optical devices and for his guidance and support. I am thankful to Dr. Li, Dr. Kumar and Dr. Chen for being my committee members. I am grateful to Dr. Kumar for his excellent courses. I would also like to express my gratitude to Haibo Liang for his extensive help and discussions all the time.

I would also like to thank Cheryl Gies for her kindly help.

Nomenclature

ϵ permittivity of dielectric

ϵ_0 permittivity of vacuum

$\mathbf{E}$ Electric field (vectorial)

$\mathbf{H}$ Magnetic field (vectorial)

μ permeability of dielectric

μ_0 permeability of vacuum

E Electric field (scalar)

H Magnetic field (scalar)

k wavenumber in dielectric

k_0 wavenumber in vaccum

n refractive index

FD   Finite Difference

PML   Perfectly Matched Layer

PRB   Perfect Reflection Boundary

Contents

6 Conclusion   **73**

List of Figures

xi

List of Tables

Chapter 1

Introduction

1.1 Backgrounds

The increasing demand of high bandwidth, low latency and low power consumption in areas of communications and integrated systems provide great opportunities for optical devices. The advancements of optical devices analysis, design and fabrication in turn requires the simulation processes to be both rigorous and efficient. In the area of waveguide modeling, Mode Matching Method (MMM) is popular for its simplicity and straight, and much more efficient when comparing with time domain methods like Finite-Difference Time Domain (FDTD) method. The process usually requires the determination of a complete mode set. One of the possible approaches is Finite-Difference (FD) based mode solver, with Perfectly Matched Layers as boundary conditions.

However, one of the drawbacks of Mode Matching Method is that large number of modes

are involved in the process in order to get relatively accurate results, especially for structures with significant radiation effects like in the case of bending structures and second-order gratings etc.

1.2   Contributions

To address the problem mentioned above, an Improved Mode Matching Method is proposed to improve numerical stability and speed up convergence. Besides, the Perfectly Matched Layer framework for asymmetric structures is improved with the introduction of Weighted Optical Path Distance, which provides better numerical results for asymmetric structures. Typical waveguide structures including bending structures, straight-bending-straight structures, long-period gratings, gratings with deposited layers and gratings with strong index corrugations are investigated and analyzed using the above approaches.

This thesis is organized in the following manner. Chapter 2 summaries the basic theories about waveguide simulation. Governing equations, i.e., Maxwell Equations, are reduced to simple second-order differential Helmholtz equations using scalar approximation, which serves as basic starting point of analyzing passive devices. Basic scheme of Finite-Difference method is explained and higher order schemes are summarized. Boundary condition, i.e., Perfectly Matched Layer, is introduced from the point of theory as well as implementation. Weighted Optical Path Distance is proposed to improve numerical precision for asymmetric structures. Chapter 3 reviews conventional Complex Mode Matching Method and provides better expansion formula based on matrix optimization. Chapter 4 talks about the application of Mode Matching Method to bending structures.

Bending structures with different radiuses are investigated and analyzed. Important roles of high order complex modes in energy transfer is revealed in structures of small radii. Chapter 5 provides the simulation results of several typical gratings using Mode Matching Method, with the comparison of Coupled Mode Theory. Chapter 6 wraps up the work and talks about possible improvements and work directions in the future.

Chapter 2

Complex Modes

The process of waveguide simulation and analysis relies on the determination of a complete mode set from governing equations. Of all the proposed approach, Finite-Difference Method (FDM) based method is by far the most popular for its simplicity and straightforwardness. In practice, however, to improve accuracy one step further and accelerate convergence, higher order finite-difference based schemes are commonly used.

Due to the nature of numerical simulation, boundary conditions must be chosen carefully. Simple boundary conditions, like Perfect Reflection Boundary (PRB), are relatively easy to be implemented, but are not in coherence with reality. To address the problem , complicated boundary condition, Perfectly Matched Layer (PML) [1] [2], is introduced. To validate the numerical results, the parameters of the PML is altered, showing the convergence within the PML framework itself as well as convergence to real world structure.

2.1   Scalar Approximation

Before starting the discussion, the following assumption are made: i) the electro-magnetic waves propagates in source-free, lossless, piece-wise isotropic dielectrics, which is true for most photonic devices, ii) the time parameter is eliminated, i.e. only frequency domain is considered.

Under those assumptions, the governing equations, i.e., Maxwell equations, are written as [3]

$$\nabla \times \mathbf{E} = -j\omega\mu_0\mathbf{H}$$

$$\nabla \times \mathbf{H} = j\omega\epsilon_0 n^2\mathbf{E}$$

$$\nabla \cdot \mathbf{E} = 0$$

$$\nabla \cdot \mathbf{H} = 0$$

(2.1)

in which $\mathbf{E}$, $\mathbf{H}$ are vectorial electric and magnetic fields, respectively, with $n = n(x, y, z)$ the refractive index of the dielectric, $\epsilon = \epsilon_0 n^2$ the permittivity of the dielectric, μ_0, ϵ_0 the permittivity and permeability of vacuum.

By separating transverse and propagating components, the governing equation could be reduced to

$$\nabla_t^2\mathbf{E}_t + (k_0^2 n^2 - \beta^2)\mathbf{E}_t = \nabla_t\left[\nabla_t \cdot \mathbf{E}_t - \frac{1}{n^2}\nabla_t \cdot (n^2\mathbf{E}_t)\right]$$

(2.2)

This is often referred as full-vector form of the governing equations, since it includes both

transverse components of the field [4].

More often than not, it is sufficient to solve one component. Follow this simplicity, let E denote one of the field components, and neglect the coupling between the two polarizations, the full-vector equation becomes

$$\frac{\partial^2 E}{\partial x^2} + (k_0^2 n^2 - \beta^2)E = 0 \tag{2.3}$$

This procedure is referred as scalar approximation. The expression is known as scalar equation or semi-vector equation, which takes the form of an Helmholtz equation. The solutions associated with the previous equation are Transverse Electric (TE) modes.

The same procedure could be applied to **H** field

$$n^2 \left[\frac{\partial}{\partial x} \left(\frac{1}{n^2} \frac{\partial H}{\partial x} \right) \right] + (k_0^2 n^2 - \beta^2)H = 0 \tag{2.4}$$

The is the scalar governing equation for magnetic field. The solutions associated are Transverse Magnetic (TM) modes.

Once solving the above differential equation, the other filed components could be easily dissolved. Suppose the E component of TE mode is ready, then

$$H_x = \frac{\beta}{\omega\mu_0}E_y$$

$$H_y = -\frac{\beta}{\mu\epsilon_0}E_x \qquad\qquad (2.5)$$

$$H_z = \frac{j}{\omega\mu_0}\Big(\frac{\partial E_y}{\partial x} - \frac{\partial E_x}{\partial y}\Big)$$

For TM mode,

$$E_x = -\frac{\beta}{\omega\epsilon_0 n^2}H_y$$

$$E_y = \frac{\beta}{\omega\epsilon_0 n^2}H_x \qquad\qquad (2.6)$$

$$E_z = \frac{1}{j\omega\epsilon_0 n^2}\Big(\frac{\partial H_y}{\partial x} - \frac{\partial H_x}{\partial y}\Big)$$

2.2 Finite-Difference Method

The FDM was firstly introduced into area of optical devices simulation by Stern in 1988 [5]. According to Stern's propose, the second-order derivatives is approximated using basic three-point difference scheme, while the discontinuity of the medium is matched by averaging refractive indices across interface.

$$
\begin{array}{ccc}
\psi_{i-1} & \psi_i & \psi_{i+1} \\
\bullet & \bullet & \bullet \\
x-h & x & x+h
\end{array}
$$
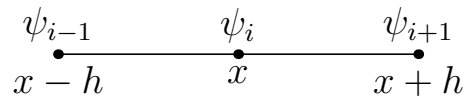
Figure 2.1: Basic Finite Difference scheme

Consider the scheme shown in Figure 2.1, ψ_{i-1}, ψ_i, ψ_{i+1} are electric or magnetic fields at locations of $x-h$, x, $x+h$, respectively, with h as step size of the uniform mesh. The

7

second-order derivatives could be approximated as

$$\frac{\partial^2 \psi_i}{\partial x^2} = \frac{\psi_{i-1} - 2\psi_i + \psi_{i+1}}{h^2} + O(h^3) \tag{2.7}$$

Thus the scalar equations (Equation 2.3 and Equation 2.4) shall be discretized as

$$\frac{1}{h^2}\left(\psi_{i-1} - 2\psi_i + \psi_{i+1}\right) + n_i^2 k_0^2 \psi_i = \beta^2 \psi_i \quad \text{(TE)}$$

$$\frac{n_i^2}{h^2}\left(\frac{1}{n_{i-}^2}\psi_{i-1} - (\frac{1}{n_{i-}^2} + \frac{1}{n_{i+}^2})\psi_i + \frac{1}{n_{i+}^2}\psi_{i+1}\right) + n_i^2 k_0^2 \psi_i = \beta^2 \psi_i \quad \text{(TM)} \tag{2.8}$$

in which

$$n_{i-} = \frac{1}{2}(n_{i-1} + n_i)$$

$$n_{i+} = \frac{1}{2}(n_i + n_{i+1}) \tag{2.9}$$

Combining all the sampling points and rewrite the equation into matrix form

$$\mathbf{A}\Psi = \beta^2 \Psi \tag{2.10}$$

where $\mathbf{A}$ is a tri-diagnonal matrix. Once solving the equation, the eigenvalues would be β^2, while the eigenvectors would be mode profiles, thus the problem of generating mode set is transformed into an eigenvalue solving problem.

The scheme showed above is extremely easy to implement, yet the results are relatively

less accurate. One reason is that the scheme adopts a three-point stencil. Secondly, interface conditions at refractive index discontinuities are over simplified. The truncation error of this scheme is $\mathbf{O}(h)$, where h is the mesh size. Although the accuracy could be improved by using finer meshes, the overhead of computation would be significant. Other schemes have be proposed over the years to address the problem. Vassallo [6] provided an improved scheme with $\mathbf{O}(h^2)$ truncation error by setting interfaces at middle of sampling points and expanding Taylor series at refractive index discontinuities. Further, Chiou [7] expanded the work by introducing the Generalized Douglas operator. The truncation error was reduced to $\mathbf{O}(h^4)$, irrespective of the location of interfaces. Until recently, arbitrary precision scheme was proposed by Chiou [8], that is, any higher order scheme could be achieved by using wider stencil and higher order interface conditions. The implementation accompanying this thesis adopts Chiou's scheme using a five-point stencil, which has a $\mathbf{O}(h^4)$ truncation error.

2.3   Boundary Conditions

To illustrate the FDM and PML framework, a 1D computation model is shown as Figure 2.2. The innermost is a core layer, clamped by cladding 1 and cladding 2 (also referred as substrate and cover), of which the refractive index of core layer is usually higher than its neighbors. There might be multiple groups of core-cladding layers. The PML layers are placed at outer part, with PRB terminating the computation grid.

Perfect Reflect Boundary (PRB) terminate the computation window, which internally requires field amplitude at boundaries to be zero. This practice relies on the fact that the
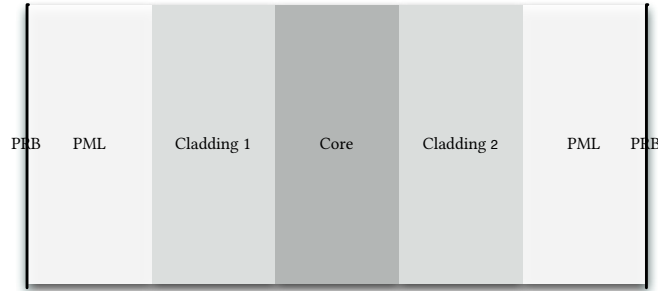
Figure 2.2: Computation model. Perfectly Matched Layers (PMLs) are placed at outermost while Perfect Reflection Boundary (PRB) terminate the computation grid.

guided mode will always decay to zero with large enough computation window. However, parasite reflections may happen for radiative waves and therefore affect the simulation results. Further, larger computation window means more computation resources are required to complete the process. To address the problems, Perfectly Matched Layers (PML) is introduced.

PMLs are artificial anisotropy materials. The field propagation in PMLs are governed by modified Maxwell's equations, [1]

$$\nabla \times \mathbf{E} - j\beta \mathbf{E} = -j\omega\mu\Lambda\mathbf{H}$$
$$\nabla \times \mathbf{H} - j\beta \mathbf{H} = j\omega\epsilon\Lambda\mathbf{E}$$

(2.11)

in which $\epsilon(x, y)$ is the refractive index. The tensor Λ is given by

$$\Lambda = \begin{bmatrix} S_y S_z / S_x & 0 & 0 \\ 0 & S_x S_z / S_y & 0 \\ 0 & 0 & S_x S_y / S_z \end{bmatrix} \tag{2.12}$$

in which S_x and S_y are called coordinate stretching factors and are given as

$$S_x = 1 + \frac{\sigma_x}{j\omega\epsilon}$$
$$S_y = 1 + \frac{\sigma_y}{j\omega\epsilon} \tag{2.13}$$
$$S_z = 1 + \frac{\sigma_z}{j\omega\epsilon}$$

where σ_x, σ_y are absorption parameters, along x, y and z directions, respectively.

The coefficients σ are crucial to effectively reduce parasite reflections from the PRB. One of the commonly used absorption profiles is

$$\sigma = \sigma_{max} \left(\frac{\rho}{T_{PML}} \right)^m \tag{2.14}$$

in which T_{PML} is PML thickness and ρ is the distance measured from the starting point of PML. When $m = 2$, the PML is most effective. Using this profile, the reflection coefficient of the PML is

$$R_{PML} = \exp\left[-\frac{2\sigma_{max}}{n\sqrt{\epsilon_0/\mu_0}} \int_0^{T_{PML}} \left(\frac{\rho}{T_{PML}} \right)^m \right] \tag{2.15}$$

11

which is the main measurement for effectiveness of the PML.

Alternatively, given reflection coefficient, the PML profile could be constructed as

$$S = 1 + \frac{\lambda}{j4\pi n T_{PML}} \left[(m+1) \ln \frac{1}{R_{PML}} \right] \left(\frac{\rho}{T_{PML}} \right)^m \tag{2.16}$$

To simply the incorporation of PML into FDM framework, introduce the complex coordinate as [2]

$$\tilde{x} = \int_0^x S_x(x') \mathrm{d}x'$$
$$\tilde{y} = \int_0^y S_y(y') \mathrm{d}y' \tag{2.17}$$

Within such a complex coordinate system, the governing equations with PML layers stay the same as scalar approximation Equation 2.3 and Equation 2.4.

2.4 Mode Orthoganlity

Let m, n be two mode indices, it is proved that the transverse modes satisfy the following relation,

$$\iint_A \left(\mathbf{E}_{tm} \times \mathbf{H}_{tn} \right) = 0 \qquad \text{for } m \neq n \tag{2.18}$$

Here is a simplified derivation. For TE modes, there exists three non-zero components,

i.e., E_y, H_x, H_z. The modified governing equation with PML layers is

$$\frac{1}{S_x}\frac{\partial}{\partial x}\frac{1}{S_x}\frac{\partial}{\partial x}E_y + (k^2 - \beta^2)E_y = 0 \tag{2.19}$$

and $H_x = \frac{S_x\beta}{\omega\mu}E_y$, thus

$$\int_0^L E_{ym}H_{xn}\mathrm{d}x = \frac{\beta_n}{\omega\mu}\int_0^L E_{ym}S_x E_{yn}\mathrm{d}x \tag{2.20}$$

and

$$
\begin{aligned}
\int_0^L E_{ym}S_x E_{yn} &= \frac{1}{\beta_m^2 - k^2}\int_0^L \frac{\partial}{\partial x}\frac{1}{S_x}\frac{\partial}{\partial x}E_{ym}E_{yn}\mathrm{d}x \\
&= \frac{1}{\beta_m^2 - k^2}\Big[\frac{1}{S_x}\frac{\partial}{\partial x}E_{ym}E_{yn} - \int_0^L \frac{1}{S_x}\frac{\partial}{\partial x}E_{ym}\frac{\partial}{\partial x}E_{yn}\mathrm{d}x\Big] \\
&= \frac{1}{k^2 - \beta_m^2}\int_0^L \frac{1}{S_x}\frac{\partial}{\partial x}E_{ym}\frac{\partial}{\partial x}E_{yn}\mathrm{d}x \\
&= \frac{1}{k^2 - \beta_n^2}\int_0^L \frac{1}{S_x}\frac{\partial}{\partial x}E_{yn}\frac{\partial}{\partial x}E_{ym}\mathrm{d}x
\end{aligned}
\tag{2.21}
$$

From the last two lines of the above formula plus the fact that $\beta_m \neq \beta_n$ when $m \neq n$, there exists

$$\int_0^L E_{ym}H_{x_n} = 0 \qquad \text{for } m \neq n \tag{2.22}$$

Parameter	Value
core refractive index n_{co}	2.0
core thickness d_{co}	2.0 μm
cladding refractive index n_{cl}	1.0
cladding thickness d_{cl}	1.0 μm
working wavelength λ	1.5 μm
PML thickness d_{PML}	1.0 μm
PML reflection coefficient R_{PML}	10^{-4}
mesh size	50 μm^{-1}

Table 2.1: Parameters used in the slab waveguide simulation

If the modes are further normalized by power, then the modes satisfy

$$\int\int_A \mathbf{E}_m \times \mathbf{H}_n = \delta_{mn} \tag{2.23}$$

where δ_{mn} is Kronecker delta.

2.5   Numerical Results and Validation of Mode Solvers

Consider a symmetric one dimensional computation model shown in Figure 2.3. The parameters used in the simulation are listed in Table 2.1.

It is noted that while the parameters of waveguide itself is fixed once the computation model is selected, the choice of parameters for PML, i.e. the PML thickness and reflection
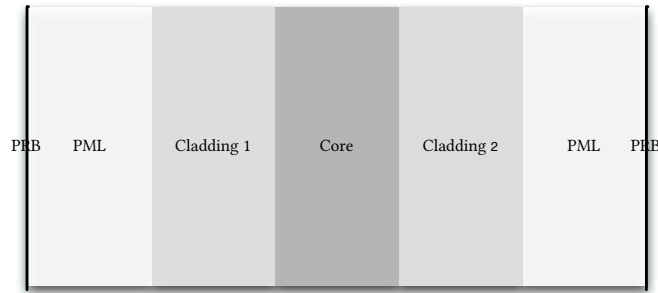
Figure 2.3: Illustration of a semmetric slab waveguide computation model

coefficient, is flexible, as long as the reflection back from PRB is negligible. The effect of different PML parameters to results will be discussed in details later in this section.

The numerical output for TE modes are shown below. Figure 2.4 reveals distributions of effective indices of first 100 modes. As it shows, the effective indices of guided modes are not effected as pure real numbers, while effective indices of the radiation modes are discretized and scattering in fourth quadrant of complex plane. It is noted that real part of the complex refractive index could be smaller than 1. This does not mean that the light speed will be larger than c since the imaginary part is significant. This behavior is like the situation when light propagating in the metal. Figure 2.5 plots profiles (actually amplitude of $\mathbf{E}_y$) of first 3 guided modes, and Figure 2.6 profiles of 3 complex modes. It is clear that for lower order modes, the energy is concentrated mainly in core layers, while for higher order modes, the energy is more evenly distributed in core layers, claddings layers as well as PML layers. It is also noted that for much higher order layers, most energy leaks to PML layers, but the waves decay dramatically as propagating into PML layers, becoming effectively zero at the end of the PML layers, i.e. PRB. Profiles of the complex modes show clearly the purpose of PML layers and justify the effectiveness of them. Orthogonality of
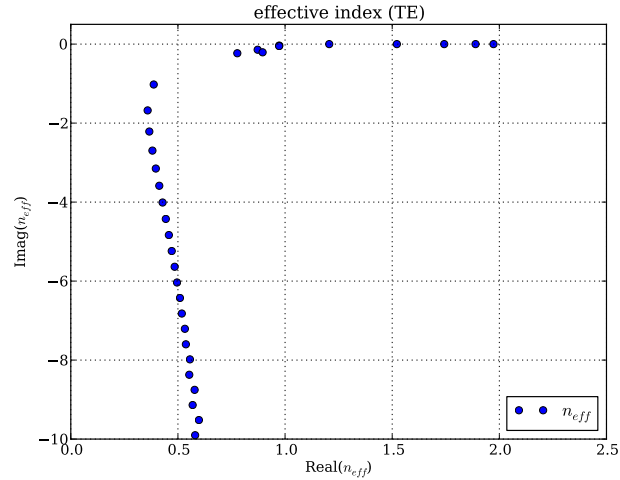
Figure 2.4: Effective indices of TE modes

modes are visualized in Figure 2.7.

Similar results apply for TM modes.

In order to validate the PML framework, a few routines could be adopted in the calculation process.

Firstly, the step size of grid could be varied to reveal whether the numerical computation process itself is stable and convergent. Figure 2.8, Figure 2.9 and Figure 2.10 show how effective indices of guided modes and complex modes changes with regard of step size of computation grid. As the step size decreases, i.e., the mesh size increases, the numerical results stabilizes and converges.

Same verification routines could be applied to TM modes.

Secondly, parameters of the PML layers might be changed to reveal how close the models

Figure 2.5: Profiles of first 3 guided modes (TE)

Figure 2.6: Profiles of 3 complex modes (TE)

17

Orthogonality (TE)

Figure 2.7: Orthogonality of Modes (TE)

Figure 2.8: Effective index of guided mode (m = 1) vs. stepsize (TE)
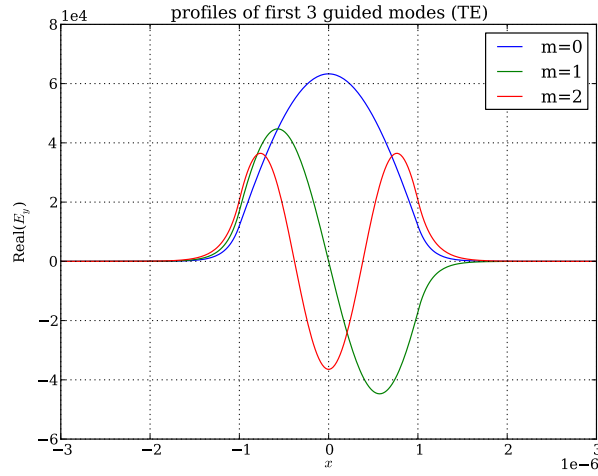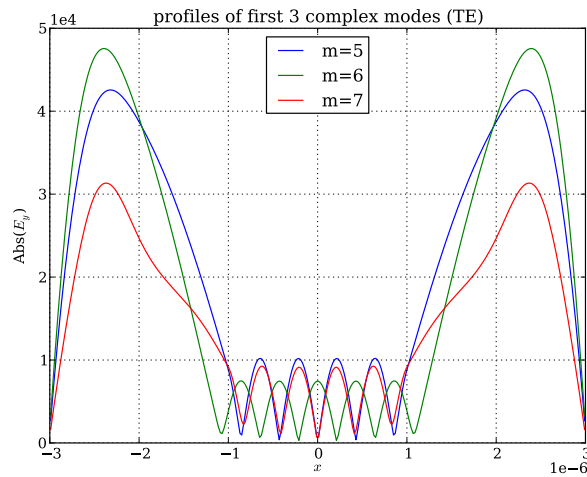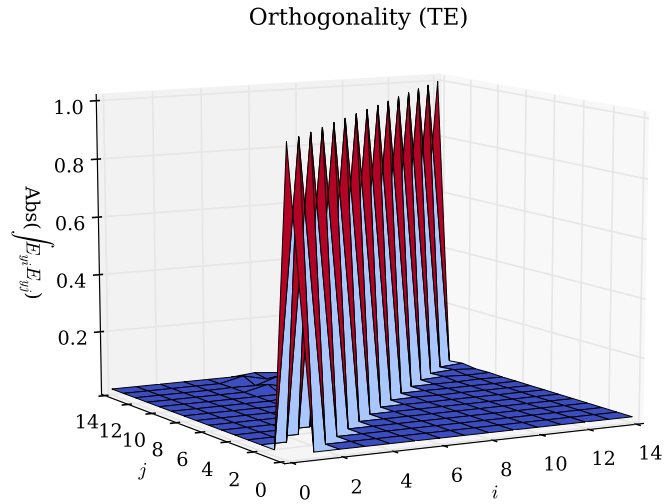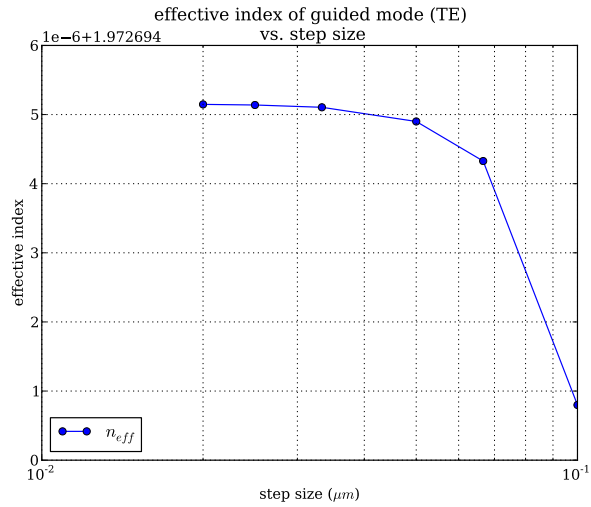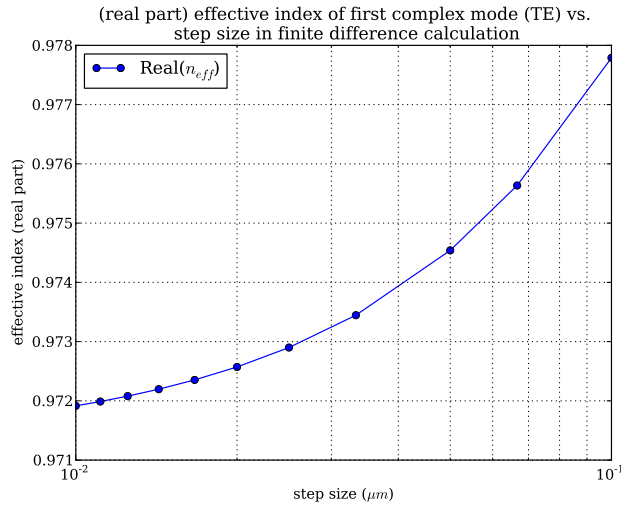
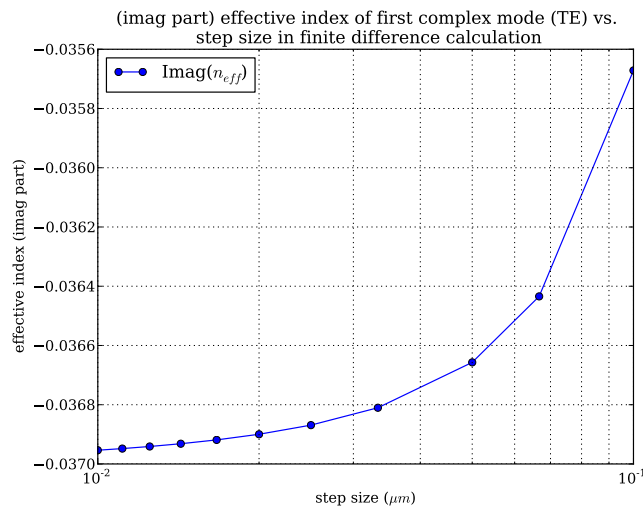Figure 2.9: Effective index of complex modes (real part) vs. stepsize (TE)

Figure 2.10: Effective index of complex modes (imaginary part) vs. stepsize (TE)

with PML layers when compared to real world structures. The thickness, d_{PML}, and reflection coefficient, R_{PML}, are two key parameters to PML layers. Due to the approaches of numerical implementation, only R_{PML} are manipulated. Figure 2.11 shows how effective indices of modes are affected by reflection coefficient of PML layer. The effective indices of guided modes remains un-effected regardless of PML parameters, while the effective indices of complex modes are highly sensitive. When R_{PML} equals to 1, the computation model is actually PRB models. The effective indices of guided modes locates on x-axes while radiation modes are discretized and are pure imaginary complex numbers. With these settings, the computation model is most away from real world structure. As R_{PML} decreases, the computation model get closer to real world structure. The complex modes shift to right part of the plane and start to split. More branches emerges as R_{PML} becomes smaller. One notable fact is that one of the branches stabilizes when R_{PML} becomes significant small. This specific branch is called the quasi-leaky branch. So far the modes are divided into three categories, the guided modes, the quasi-leaky modes and the PML modes. Guided modes and quasi-leaky modes are internally supported by the structure itself, thus remains un-affected with parameters of PML layers, as shown in Figure 2.12 and Figure 2.13. While for PML modes, energy of the waves mostly resides in PML layers, thus highly sensitive to changes of PML parameters, as shown in Figure 2.14, Figure 2.15 and Figure 2.16. The choice of PML parameters is empirical. When the reflection coefficient relatively large (close to 1), which means large portion of the waves will be reflected back to cladding layer, the computation model is most divergent from real word structure. While when the reflection coefficient is relatively small (close to 0), the floating-point truncation error will be significant, causing problem in convergence processes.

Similar results applies to TM case.
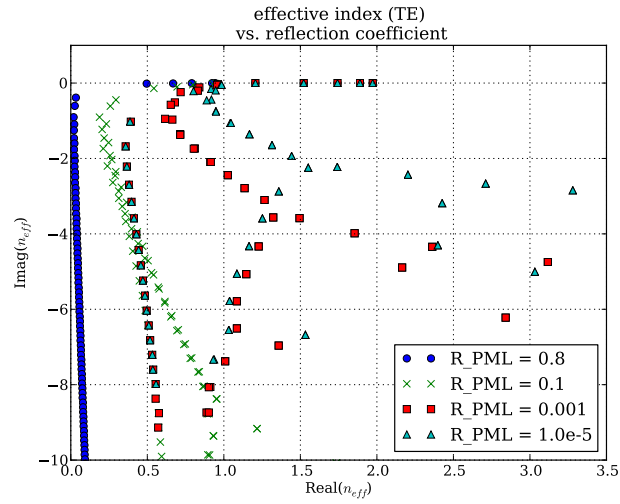
Figure 2.11: Effective indices vs. R_{PML} (TE)
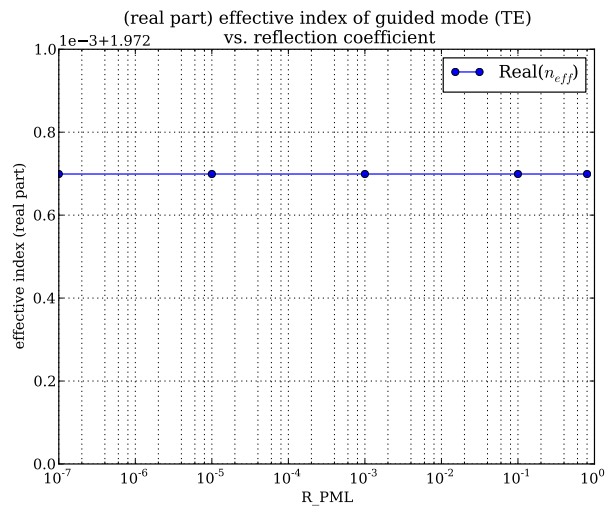
Figure 2.12: Effective index of guided modes vs. R_{PML} (TE)
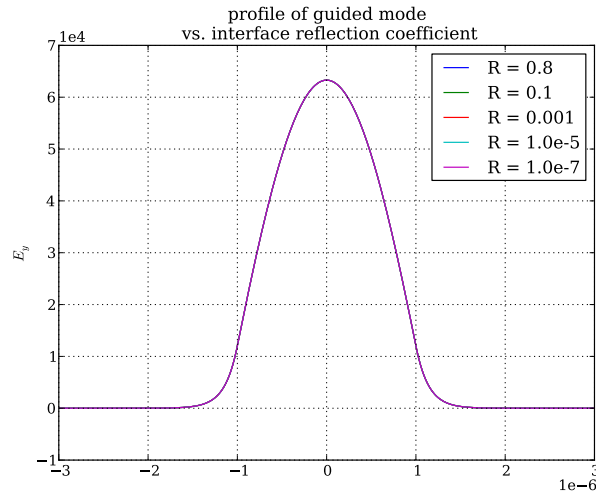
Figure 2.13: Profiles of guided modes vs. R_{PML} (TE)
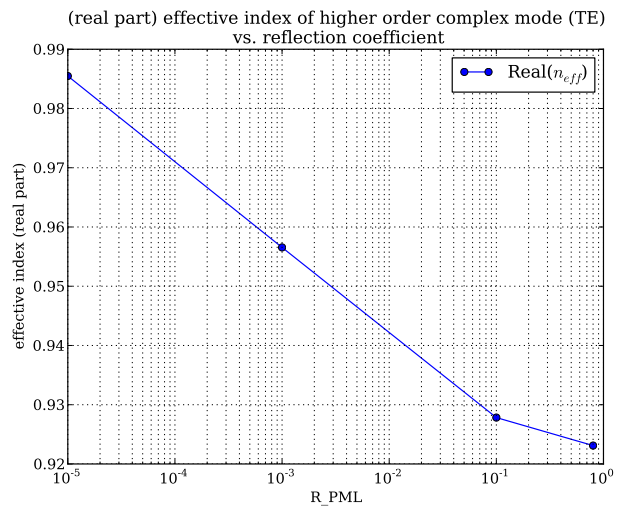
Figure 2.14: Effective index of complex modes (real part) vs R_{PML} (TE)
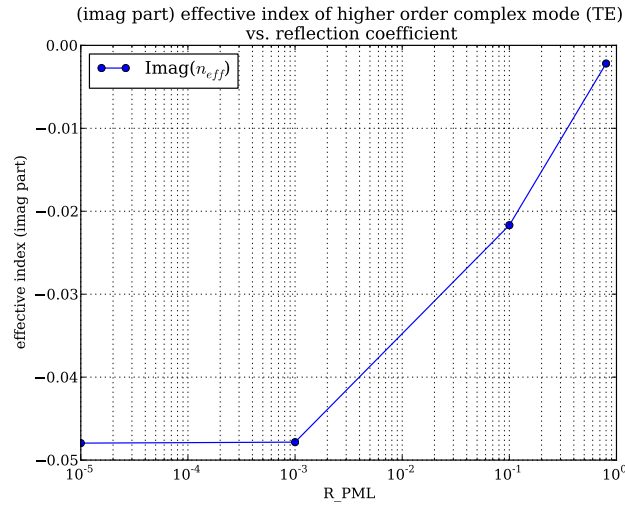
Figure 2.15: Effective index of complex modes (imaginary part) vs R_{PML} (TE)
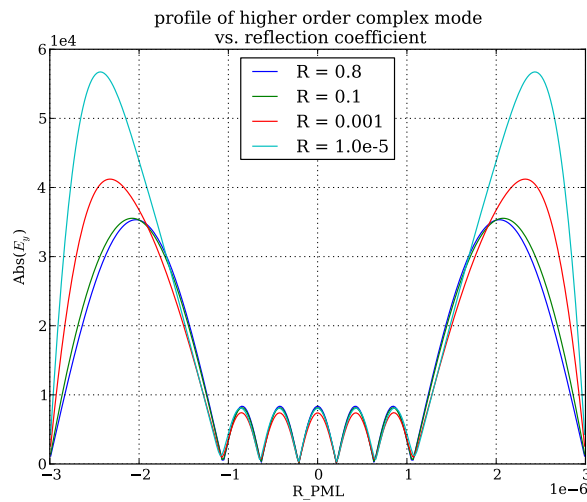
Figure 2.16: Profiles of complex modes vs R_{PML} (TE)

2.6 Weighted Optical Path Distance

Problem arises when dealing with asymmetric waveguide structures. The Berenger modes will split into two branches, namely S-Berenger modes (Substrate-Berenger modes) and C-Berenger modes (Cladding-Berenger modes), which have different phase angles. These high order modes cause convergence problem in mode matching since the integral overlap between these modes and guided modes are usually small which makes the coefficient matrix becomes singular. The phase angles of Berenger modes are highly depend on parameters of structures and PMLs. Thus adjustments could be made to avoid the splitting of Berenger Modes [9]. This method could help to reduce numerical fluctuations and speed up convergence process in Mode Matching Method.

Suppose $n_{eff,n}$ is the effective index of m-th Berenger mode, and $n_{eff} = |n_{eff}|e^{-j\theta_n}$, where θ is the phase angle. For high order Berenger mode, there is approximation,

$$\lim_{n \to \infty} n_{eff,n} = \infty$$
$$\lim_{n \to \infty} \theta_n = \theta_0 \tag{2.24}$$

where $0 < \theta_0 < \frac{\pi}{2}$. The phase angles for S-Berenger mode and C-Berenger mode are approximated by [10]

$$\tan \theta_0^{s,c} = -2k_0 \frac{\varphi_{s,c}}{\ln R_{PML,(s,c)}} \tag{2.25}$$

in which $\varphi = \int nx\mathrm{d}x$ is the optical path distance in substrate or cladding with PML layers.

Parameter	Value
refractive index of Si	3.47
refractive index of SiO$_2$	1.44
refractive index of Ge	4.1
core thickness	0.22 μm
cladding thickness	0.5 μm
working wavelength λ	1.55 μm
PML thickness d_{PML}	2.0 μm

Table 2.2: Parameters used in photon-detector simulation

It is clear that the phase angles of the Berenger modes are affected by two factors, that is, the reflection coefficient of PML layers R_{PML} and the optical path distance φ. Thus the PML reflection coefficient could be adjusted according to the the optical path distance to ensure same phase angles in S-Berenger modes and C-Berenger modes.

To demonstrate the effectiveness of the weighted optical path distance technique, we simulated a photon-detector structure, as shown in upper right corner of Figure 2.17. TE light is launched from silicon slab waveguide into a Germanium photodetector. The parameters used in the simulation are listed in Table 2.2.

In case of Unadjusted Optical Path Distance (conventional approach, referred as UOPD below), the PML reflection coefficients are set to 5×10^{-3} in both substrate and cladding side. For Weighted Optical Path Distance (referred as WOPD below), the reflection coefficient in cladding side is set to 5×10^{-3}, while the reflection coefficient in substrate side is adjusted to 2.8×10^{-7} to ensure same phase angle in S-Berenger modes and C-Berenger modes.
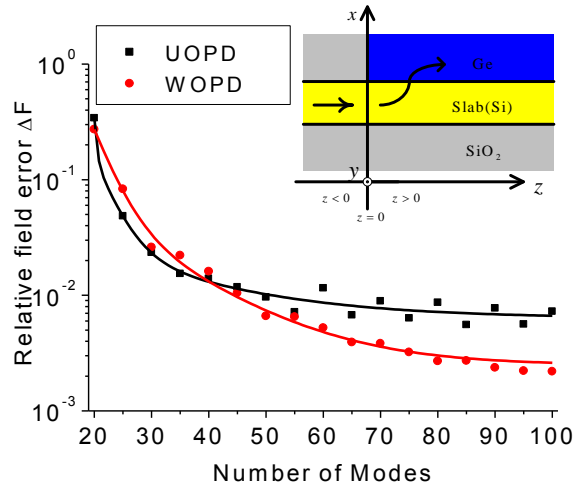
Figure 2.17: Comparision of convergence speed in Mode Matching Method between Unadjusted Optical Wave Path (UOPD) and Weighted Optical Wave Path (WOPD)

As shown in Figure 2.18 UOPD S-Berenger modes and C-Berenger modes are splitting with different angles, while in case of WOPD, they share the same asymptote angle. Also shown in in the figure are the mode profiles of 81-th and 82-th modes. In case of UOPD, most energy is concentrated in cladding side, making the mode profiles much smaller in the other side, which results in more errors in numerical computation. While the energy in WOPD is more evenly distributed.

Figure 2.17 compares the convergence speed in Mode Matching Method between Unadjusted Optical Wave Path (UOPD) and Weighted Optical Wave Path (WOPD). The y-axis is relative field matching error on the interface. It is clear that the results from WOPD suffer less fluctuations and converge more quickly.
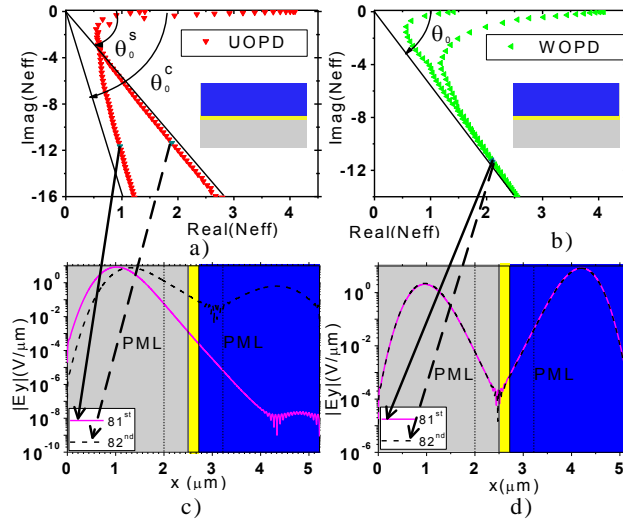
Figure 2.18: Comparision of phase angle (a, b) and mode profiles (E_y) (c, d) between Un-adjusted Optical Wave Path (UOPD) and Weighted Optical Wave Path (WOPD)

2.7   Summary

In this chapter, the governing equations for source-free waveguide are derived and explained. Scalar approximation are made to simplify simulation. Numerical simulations based on Finite-Difference Method are explained and higher order schemes are touched in brevity. As with other numerical simulations, the boundary condition must be chosen carefully to ensure validation of the simulation. Specially for the simulation of waveguides, the Perfect Matched Layers are used to inhibit wave reflections from boundaries. Thanks to the nature of numerical computation, the radiation modes are discretized such that the integration of continuous radiation modes are avoided and the complex modes could be dealt the same way as guided modes. Later on, results of an example slab waveguides are presented and analyzed. To justify the validation of computation model, a few

computation parameters are altered to show the robustness and convergence of the numerical results. A simple technique, i.e., adjusting PML reflection coefficient according to Weighted Optical Path Distance, is proposed to ensure same phase angles in Berenger modes. These works laid solid foundations for computation and analysis of more complex waveguide structures.

Though the FD method is widely used, it is far from perfect. In practice, higher order FD schemes, which means much more complex formulas, shall be adopted to achieve more precise results. The FD approach turns the problem of mode finding into eigenvalue solving problem, but most eigenvalue solvers implemented in modern software systems is implemented with convergence process as termination condition, which is time consuming and un-efficient. The computation complexity soars up and the computation time quickly becomes intolerable when computation dimension becomes larger, which becomes the main bottleneck of the FD methods.

Chapter 3

Improved Mode Matching Method

Mode Matching Method (MMM), also known as Bidirectional Eigenmode Propagation (BEP) or Eigenmode Expansion (EME), is an efficient and rigorous approach to simulate electromagnetic propagation within waveguides, especially with discontinuities along propagation direction. In MMM, the electromagnetic fields are decompose into a basis set of local eigenmodes, which is found by solving Maxwell equations in each cross section. By applying interface condition at discontinuities, both sides are related using a transfer/scatter matrix. The entire waveguide properties are calculated by cascading the transfer/scatter matrices. With the introduction of PML framework, complex modes could be treated the same way as guided modes, thus making Complex Mode Matching Method.

3.1   Conventional Mode Matching Method

Considering a wave propagating through an interface locating at $z = 0$, part of the wave will be reflected back into $z < 0$ region and part into $z > 0$ region. Given set of eigenmodes for $z < 0$ region (denoted as A), which consists of N modes, and set of eigenmodes for $z > 0$ region (denoted as B), which consists of M modes, then the forward transmission wave and backward reflection wave could be expressed as

$$
\begin{aligned}
\mathbf{E}_t^A &= \sum_{n=1}^{N} \left(a_n^+ e^{-j\beta_n z} + a_n^- e^{+j\beta_n z} \right) \mathbf{e}_{tn}^A \\
\mathbf{H}_t^A &= \sum_{n=1}^{N} \left(a_n^+ e^{-j\beta_n z} - a_n^- e^{+j\beta_n z} \right) \mathbf{h}_{tn}^A \\
\mathbf{E}_t^B &= \sum_{m=1}^{M} \left(b_m^+ e^{-j\beta_m z} + b_m^- e^{+j\beta_m z} \right) \mathbf{e}_{tm}^B \\
\mathbf{H}_t^B &= \sum_{m=1}^{M} \left(b_m^+ e^{-j\beta_m z} - b_m^- e^{+j\beta_m z} \right) \mathbf{h}_{tm}^B
\end{aligned}
\tag{3.1}
$$

where $\mathbf{E}_t^A$ denotes transverse electric fields, with $\mathbf{e}_{tn}^A$ transverse electric fields of n-th eigenmode within waveguide A, a_+ and a_- are amplitudes of forward and backward waves. The same naming conventions applies on magnetic fields as well as waveguide B.

The interface conditions require continuities of tangential components of electric and magnetic files at interfaces, i.e., $z = 0$

$$\sum_{n=1}^{N}(a_n^+ + a_n^-)\mathbf{e}_{tn}^A = \sum_{m=1}^{M}(b_m^+ + b_m^-)\mathbf{e}_{tm}^B$$
$$\sum_{n=1}^{N}(a_n^+ - a_n^-)\mathbf{h}_{tn}^A = \sum_{m=1}^{M}(b_m^+ - b_m^-)\mathbf{h}_{tm}^B \tag{3.2}$$

Define inner product of field vectors as

$$\langle \mathbf{e} \,|\, \mathbf{h} \rangle \equiv \frac{1}{2} \int \int \; (\mathbf{e} \times \mathbf{h}) \cdot \hat{z} \mathrm{d}s \tag{3.3}$$

By taking inner product of Equation 3.2 with $\mathbf{h}_{tm}^B$ and $\mathbf{e}_{tm}^B$, respectively, and utilizing orthogonal properties of eigenmode set, the modal amplitudes b_m^+ and b_m^- could be obtained as expressions of a_n^+ and a_n^-,

$$b_m^+ = \sum_{n=1}^{N} a_n^+ \Big(\frac{\langle \mathbf{e}_{tn}^A \,|\, \mathbf{h}_{tm}^B \rangle + \langle \mathbf{e}_{tm}^B \,|\, \mathbf{h}_{tn}^A \rangle}{2 \langle \mathbf{e}_{tm}^B \,|\, \mathbf{h}_{tm}^B \rangle} \Big) + \sum_{n=1}^{N} a_n^- \Big(\frac{\langle \mathbf{e}_{tn}^A \,|\, \mathbf{h}_{tm}^B \rangle - \langle \mathbf{e}_{tm}^B \,|\, \mathbf{h}_{tn}^A \rangle}{2 \langle \mathbf{e}_{tm}^B \,|\, \mathbf{h}_{tm}^B \rangle} \Big)$$
$$b_n^- = \sum_{n=1}^{N} a_n^+ \Big(\frac{\langle \mathbf{e}_{tn}^A \,|\, \mathbf{h}_{tm}^B \rangle - \langle \mathbf{e}_{tm}^B \,|\, \mathbf{h}_{tn}^A \rangle}{2 \langle \mathbf{e}_{tm}^B \,|\, \mathbf{h}_{tm}^B \rangle} \Big) + \sum_{n=1}^{N} a_n^- \Big(\frac{\langle \mathbf{e}_{tn}^A \,|\, \mathbf{h}_{tm}^B \rangle + \langle \mathbf{e}_{tm}^B \,|\, \mathbf{h}_{tn}^A \rangle}{2 \langle \mathbf{e}_{tm}^B \,|\, \mathbf{h}_{tm}^B \rangle} \Big) \tag{3.4}$$

Written in Matrix form,

$$\begin{bmatrix} \mathbf{B}_+ \\ \mathbf{B}_- \end{bmatrix} = \begin{bmatrix} \mathbf{T}_{++} & \mathbf{T}_{+-} \\ \mathbf{T}_{-+} & \mathbf{T}_{--} \end{bmatrix} \begin{bmatrix} \mathbf{A}_+ \\ \mathbf{A}_- \end{bmatrix} = \mathbf{T} \begin{bmatrix} \mathbf{A}_+ \\ \mathbf{A}_- \end{bmatrix} \tag{3.5}$$

where

$$
\begin{aligned}
\mathbf{T}_{\pm\pm}(m,n) &= \frac{\left\langle \mathbf{e}_{tn}^{A} \,\middle|\, \mathbf{h}_{tm}^{B} \right\rangle + \left\langle \mathbf{e}_{tm}^{B} \,\middle|\, \mathbf{h}_{tn}^{A} \right\rangle}{2\left\langle \mathbf{e}_{tm}^{B} \,\middle|\, \mathbf{h}_{tm}^{B} \right\rangle} \\
\mathbf{T}_{\pm\mp}(m,n) &= \frac{\left\langle \mathbf{e}_{tn}^{A}, \mathbf{h}_{tm}^{B} \right\rangle - \left\langle \mathbf{e}_{tm}^{B} \,\middle|\, \mathbf{h}_{tn}^{A} \right\rangle}{2\left\langle \mathbf{e}_{tm}^{B} \,\middle|\, \mathbf{h}_{tm}^{B} \right\rangle}
\end{aligned}
\tag{3.6}
$$

and

$$
\mathbf{T} = \begin{bmatrix} \mathbf{T}_{++} & \mathbf{T}_{+-} \\ \mathbf{T}_{-+} & \mathbf{T}_{--} \end{bmatrix}
\tag{3.7}
$$

is known as T-matrix (Transfer Matrix).

Alternatively, a_n^- and b_m^+ can be obtained as expressions of a_n^+ and b_m^-,

$$
\begin{bmatrix} \mathbf{A}_- \\ \mathbf{B}_+ \end{bmatrix} = \begin{bmatrix} \mathbf{R}_{AB} & \mathbf{T}_{BA} \\ \mathbf{T}_{AB} & \mathbf{R}_{BA} \end{bmatrix} \begin{bmatrix} \mathbf{A}_+ \\ \mathbf{B}_- \end{bmatrix} = \mathbf{S} \begin{bmatrix} \mathbf{A}_+ \\ \mathbf{B}_- \end{bmatrix}
\tag{3.8}
$$

which is known as S-matrix (Scatter Matrix).

The S-matrix and T-matrix are related as

$$
\begin{aligned}
\mathbf{R}_{AB} &= -\mathbf{T}_{--}^{-1}\mathbf{T}_{-+} \\
\mathbf{T}_{BA} &= T_{--}^{-1} \\
\mathbf{T}_{AB} &= \mathbf{T}_{++} - \mathbf{T}_{+-}\mathbf{T}_{--}^{-1}\mathbf{T}_{-+} \\
\mathbf{R}_{BA} &= \mathbf{T}_{+-}\mathbf{T}_{--}^{-1}
\end{aligned}
\tag{3.9}
$$
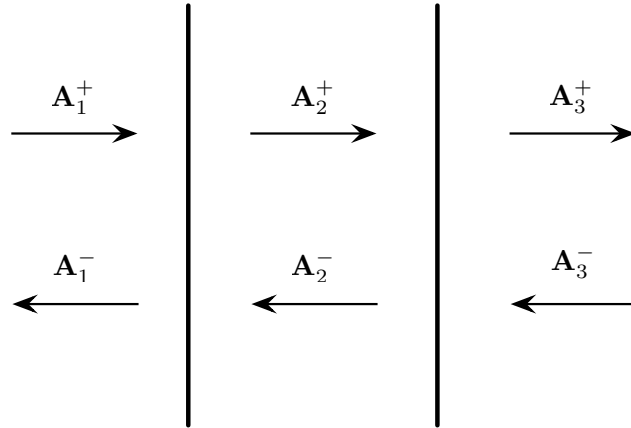
Figure 3.1: Cascade of S-matrix

For structures with multiple discontinuities, the global transfer matrix could be easily obtained by cascading every T-matrix,

$$\mathbf{T} = \mathbf{P}_n \cdot \mathbf{T}_{n,n-1} \cdot P_{n-1} \cdots \mathbf{P}_2 \cdot \mathbf{T}_{2,1} \cdot \mathbf{P}_1 \tag{3.10}$$

Where $\mathbf{P}_n$ is T-matrix within each individual waveguide section,

$$\mathbf{P}_n = \begin{bmatrix} \text{diag}(e^{-j\beta d_n}) & \mathbf{0} \\ \mathbf{0} & \text{diag}(e^{+j\beta d_n}) \end{bmatrix} \tag{3.11}$$

Things becomes slightly complicated when it comes into S-matrix since S-matrix could not be cascaded directly. Consider examples shown in Figure 3.1,

Suppose S-matrices for individual section are ready,

$$\begin{bmatrix} \mathbf{A}_1^- \\ \mathbf{A}_2^+ \end{bmatrix} = \begin{bmatrix} \mathbf{R}_{12} & \mathbf{T}_{21} \\ \mathbf{T}_{12} & \mathbf{R}_{21} \end{bmatrix} \begin{bmatrix} \mathbf{A}_1^+ \\ \mathbf{A}_2^- \end{bmatrix} \tag{3.12}$$

$$\begin{bmatrix} \mathbf{A}_2^- \\ \mathbf{A}_3^+ \end{bmatrix} = \begin{bmatrix} \mathbf{R}_{23} & \mathbf{T}_{32} \\ \mathbf{T}_{23} & \mathbf{R}_{32} \end{bmatrix} \begin{bmatrix} \mathbf{A}_2^+ \\ \mathbf{A}_3^- \end{bmatrix} \tag{3.13}$$

The overall S-matrix is

$$\begin{bmatrix} \mathbf{A}_1^- \\ \mathbf{A}_3^+ \end{bmatrix} = \begin{bmatrix} \mathbf{R}_{13} & \mathbf{T}_{31} \\ \mathbf{T}_{13} & \mathbf{R}_{31} \end{bmatrix} \begin{bmatrix} \mathbf{A}_1^+ \\ \mathbf{A}_3^- \end{bmatrix} \tag{3.14}$$

in which

$$\begin{aligned} \mathbf{R}_{13} &= \mathbf{R}_{12} + \mathbf{T}_{21}(\mathbf{I} - \mathbf{R}_{23}\mathbf{R}_{21})^{-1}\mathbf{R}_{23}\mathbf{T}_{12} \\ \mathbf{T}_{31} &= \mathbf{T}_{21}(\mathbf{I} - \mathbf{R}_{23}\mathbf{R}_{21})^{-1}\mathbf{T}_{32} \\ \mathbf{T}_{13} &= \mathbf{T}_{23}(\mathbf{I} - \mathbf{R}_{21}\mathbf{R}_{23})^{-1}\mathbf{T}_{12} \\ \mathbf{R}_{31} &= \mathbf{R}_{32} + \mathbf{T}_{23}(\mathbf{I} - \mathbf{R}_{21}\mathbf{T}_{23})^{-1}\mathbf{R}_{21}\mathbf{T}_{32} \end{aligned} \tag{3.15}$$

The complexity of cascading S-matrix is necessary since cascading of T-matrix is usually numerically unstable due to the term $\mathbf{P}_n$. When section length d_n is significant large, the term $\mathbf{P}_n$ is close to singular, making the numerical results unreliable. While S-matrix does not suffer from this problem since the cascading of S-matrix does not require P_n.

Parameter	Value
A side core refractive index n_{A1}	3.6
A side core thickness d_{A1}	0.2 μm
A side cladding refractive index n_{A2}	3.24
A side cladding thickness d_{A2}	1.0 μm
B side refractive index n_B	3.24
working wavelength λ	0.86 μm
PML thickness d_{PML}	1.0 μm
PML reflection coefficient R_{PML}	10^{-2}
mesh size	50 μm^{-1}

Table 3.1: Parameters used in wave junction simulation

In the practice of grating simulation, there usually exists thousands of periods in the structure, making the cascading of S-matrix consuming too much computation resources. The process could be accelerated by using a doubling algorithm or association reduction algorithm. That is, firstly the transfer or scatter matrix is constructed for one unit. Then the matrix for one unit is cascaded with itself to produce a matrix for two units. The new matrix is used to cascade to produce matrix for four units. And so on so forth until the overall matrix is obtained. It is obvious that the algorithm works best when period number N is exactly 2^i. When it is not the case, N could always be divided into 2^i part plus an remaining part. And the calculation of remaining part could use the same approach of division and could make use of the cached results of the larger half. It is obvious that caching the intermediate results will further accelerate the process.

Consider a wave junction shown in Figure 3.2. Parameters are listed in Table 3.1.

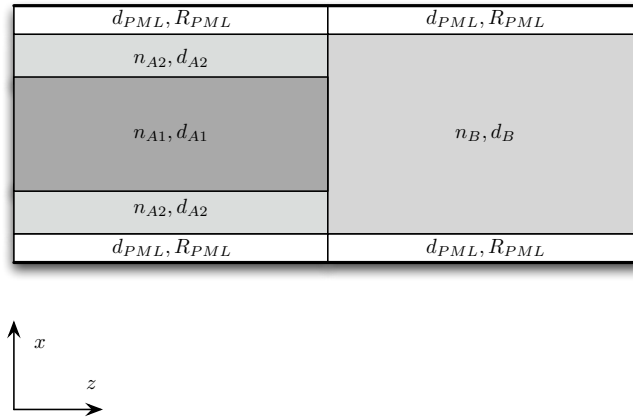| d_{PML}, R_{PML}	d_{PML}, R_{PML}
n_{A2}, d_{A2}	
n_{A1}, d_{A1}	n_B, d_B
n_{A2}, d_{A2}	
d_{PML}, R_{PML}	d_{PML}, R_{PML}

x

z

Figure 3.2: Complex Mode Matching Method computation model

Using the mode solvers implemented in the previous chapters, a set of 50 modes are obtained, as shown in Figure 3.3. Assuming fundamental mode launched from left side and no input from right side, the reflection and transmission could be calculated by solving Equation 3.5. The results are displayed in Figure 3.4. As it shows, when the wave propagate through interface, part of it transmitted and part reflected. What is more interesting is that not only fundamental mode is involved in this process but also other low order modes. And the higher order of the mode, the less it is involved. The fact that optical waves interacting with each other at interfaces is the key working principle of optical devices. Figure 3.5 shows the amplitude of electron-magnetic fields on both sides of the interface. The main fields are almost identical on both sides, which is required by the interface condition and implied by the name of the method.
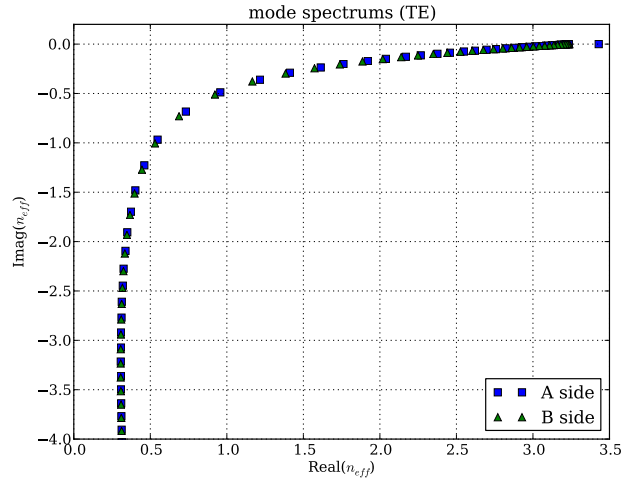
Similar results applied to TM case.
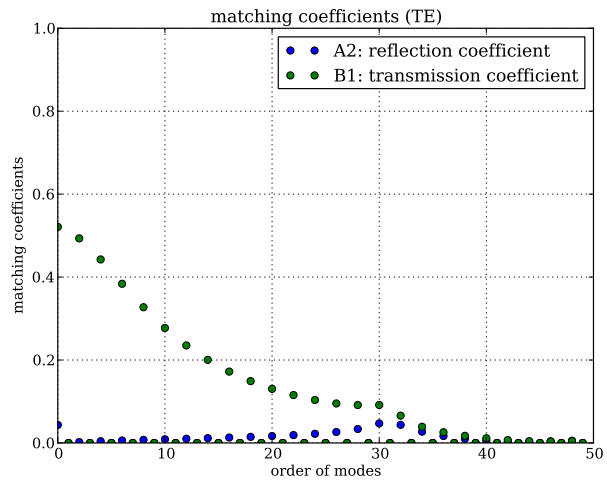
Figure 3.3: Effective indices (TE)

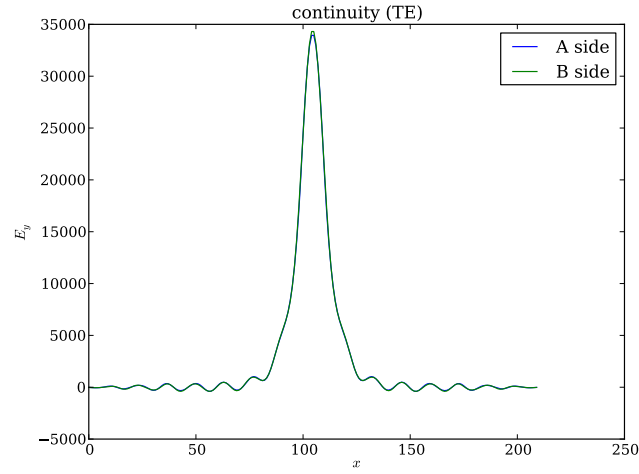Figure 3.4: Reflection and transmission (TE)

Figure 3.5: Continuity verification (TE)

3.2   Improved Mode Matching Method

Traditionally the process of Mode Matching Method requires mode orthogonality and normalization, and involves huge number of complex modes to achieve rigorous results. The truncation error might cause underestimation of radiation and crosstalk effect. Here an optimized approach is proposed to improve numerical accuracy and speedup convergence process.

Given a complete set of modes, the electric and magnetic fields are approximated by combinations of eigenmodes,

$$\mathbf{E}_t \approx \begin{bmatrix} \mathbf{e}_t, \mathbf{e}_t \end{bmatrix} \mathbf{A}$$

$$\mathbf{H}_t \approx \begin{bmatrix} \mathbf{h}_t, \mathbf{h}_t \end{bmatrix} \mathbf{A}$$

$$(3.16)$$

in which $\mathbf{e}_t$, $\mathbf{h}_t$ are electric and magnetic components of eigenmode set and $\mathbf{A}$ is defined as $[a_1^+, a_2+, \cdots, a_N^+, a_1^-, a_2^-, \cdots, a_N^-]$. Define residual field error as

$$\Delta \mathbf{E} = \mathbf{E}_t - \left[\mathbf{e}_t, \mathbf{e}_t\right] \mathbf{A}$$

$$\Delta \mathbf{H} = \mathbf{H}_t - \left[\mathbf{h}_t, \mathbf{h}_t\right] \mathbf{A}$$

(3.17)

From the perspective of energy conservation, input energy from left side should be equal to energy output to right side. Energy could be leaked out upward or downward since for an interface, the integral areas for upward and downward propagation waves are 0s. That is, the choice of $\mathbf{A}$ should make the residual power errors minimized,

$$\frac{1}{2} \int\int_S \left(\Delta \mathbf{E}^* \times \Delta \mathbf{H} + \Delta \mathbf{E} \times \Delta \mathbf{H}^*\right) \cdot \hat{z} \mathrm{d}s$$

(3.18)

This is a least square problem [12] and the optimized expression of $\mathbf{A}$ is [13]

$$\mathbf{A} = \{ \int\int_S \begin{bmatrix} -\mathbf{h}_t & \mathbf{h}_t \\ \mathbf{e}_t & \mathbf{e}_t \end{bmatrix}^H \times \begin{bmatrix} \mathbf{e}_t & \mathbf{e}_t \\ \mathbf{h}_t & \mathbf{h}_t \end{bmatrix} \cdot \hat{z} \mathrm{d}S \}^{-1} \{ \int\int_S \begin{bmatrix} -\mathbf{h}_t & \mathbf{h}_t \\ \mathbf{e}_t & \mathbf{e}_t \end{bmatrix}^H \times \begin{bmatrix} \mathbf{E}_t \\ \mathbf{H}_t \end{bmatrix} \cdot \hat{z} \mathrm{d}S \}$$

(3.19)

Figure 3.6 a silicon-on-insulator (SOI) anti-guided waveguide structure, propagating along z direction. The discontinuities appear at $z = 0$ and $z = 1$, where guided structure begins. The parameters of the structure is listed in Table 3.2.

Fundamental mode is launched at interface $z = 0$, the convergence speed is compared

Parameter	Value
refractive index of Si	3.47
refractive index of 1.44	
thickness s	1.5 μm
thickness t	0.22 μm
thickness D	3.5 μm
working wavelength λ	0.86 μm
length L	1.0 μm
PML thickness d_{PML}	3.0 μm
PML reflection coefficient R_{PML}	10^{-2}

Table 3.2: Parameters used in anti-waveguide simulation

between Conventional Mode Matching Method and Improved Mode Matching Method in Figure 3.7. It is clear that the Improved Mode Matching Method has smaller residual field error and converges more quickly, which means Improved Mode Matching Method would require much less number of mode when doing mode expansion thus saves computation resources.

3.3   Summary

In this chapter, the Mode Matching Method is derived and explained. Both T-Matrix and S-Matrix are covered, as well as approaches to deal with structures of multiple interfaces. An example computation model is provided to verify the validation of the method. Then, an improved approach of Mode Matching Method is proposed to speed up convergence
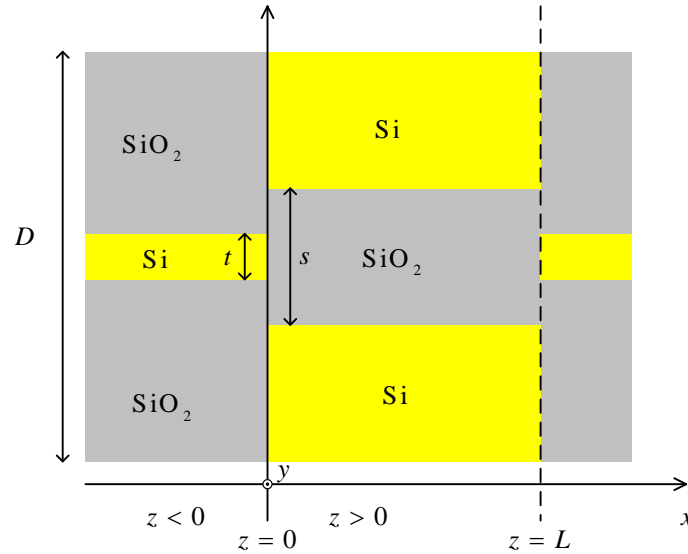
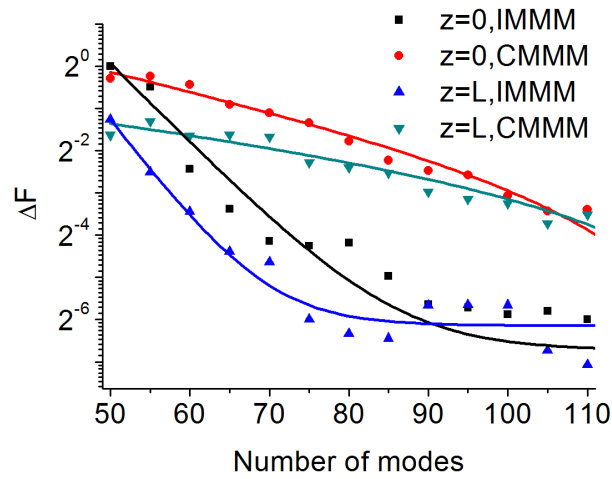Figure 3.6: Silicon-on-insulator anti-guided waveguide

Figure 3.7: Comparison of convergence between Conventional Mode Matching Method (CMMM) and Improved Mode Matching Method (IMMM). The IMMM speeds up convergence process and provides more accurate results.

when doing mode expansion. The numerical results show that improved formula converges more quickly and provides better results.

Chapter 4

Bending Structure Simulation

This chapter talks about the simulation of bending structures using Mode Matching Method. The bending structures are widely used in multimode interference devices and power splitters, but are difficult to investigate using analytical solutions due to the fact that high order radiation modes play important roles in the transmitting process. While with the introduction of PML framework, Mode Matching Method could simulate bending structures accurately if given complete set of modes. In this chapter, the mode solving problem in bending structures is firstly transformed into conventional slab structures mode solving problem, then simulation process and analysis results are presented.
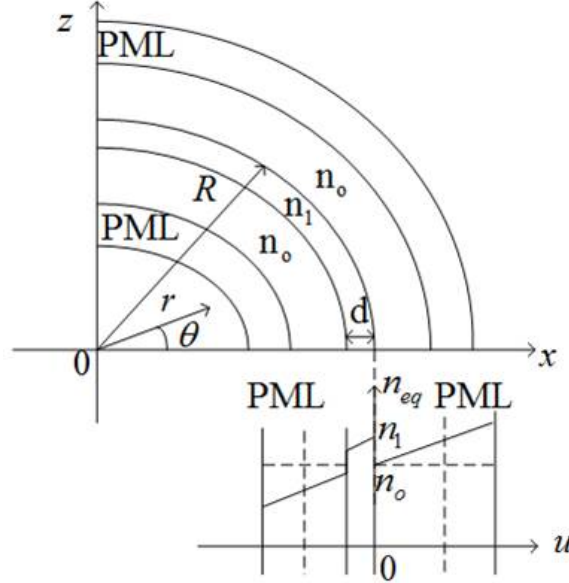
Figure 4.1: Illustration of bending structure and how to map bending structure to planar waveguide

4.1   Complex Mode Solver for Bending Structure

Figure 4.1 shows a typical bending structure of bending radius R. The core layer of refractive index n_1 is clamped by cladding layers of refractive index n_0. PML and PRB are closing the structure as numerical boundary conditions. The modified governing equations with PMLs are

$$\frac{1}{S_r}\frac{r}{R}\frac{\partial}{\partial r}\frac{1}{S_r}\frac{r}{R}\frac{\partial}{\partial r}E_y + (n^2 k_0^2 \frac{r^2}{R^2} - \beta^2)E_y = 0 \quad \text{(TE)}$$

$$\frac{1}{S_r}\frac{r}{R}\frac{\partial}{\partial r}\frac{1}{S_r}\frac{r}{R}\frac{\partial}{\partial r}H_y + (n^2 k_0^2 \frac{r^2}{R^2} - \beta^2)H_y = 0 \quad \text{(TM)}$$

$$(4.1)$$

This step-index bending structure could be mapped into a planar waveguide using confor-mal transformation [14], shown as Figure 4.1. The coordinate and index transformation are described as

$$u = R \ln \frac{r}{R}$$
$$n_{eq} = n(r)e^{u/R}$$

(4.2)

For the PML layers, the complex coordinates are introduced as

$$\hat{u} = \int S_u \mathrm{d}u$$

(4.3)

Using the conformal and complex transformation, the governing equation Equation 4.1 becomes similar to ordinary planar waveguides,

$$\frac{\partial^2 E_y}{\partial \hat{u}^2} + (n_{eq}^2)k_0^2 - \beta^2)E_y = 0$$
$$\frac{\partial^2 H_y}{\partial \hat{u}^2} + (n_{eq}^2)k_0^2 - \beta^2)H_y = 0$$

(4.4)

Thus the previous Finite-Difference based complex modes solvers could be used with little modification of index profiles.
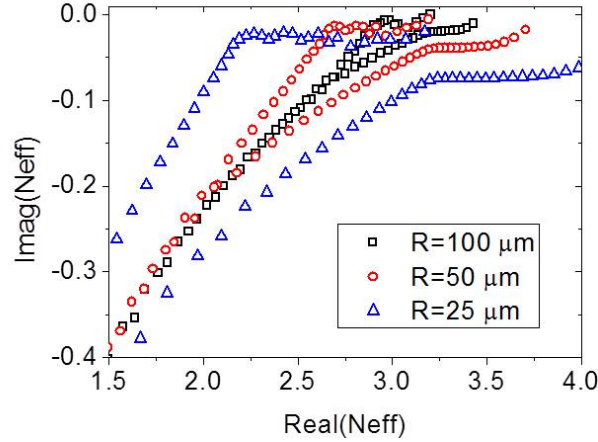
Figure 4.2: Effective indices with relatively large bending radius

4.2   Analysis of Complex Modes in Bending Structure

A bending structure with different bending radiuses is investigated using the above method. The core refractive index is 3.24, with cladding refractive index 3.18, core thickness 3 μm, inner cladding thickness 3 μm, outer cladding thickness 5 μm. The inner PML thickness is 3 μm and outer PML thickness is 5 μm, with PML reflection coefficient 10^{-8}.

Figure 4.2 and Figure 4.3 shows mode effective indices with different bending radiuses. As the radius decreases, the Berenger modes starts splitting into two branches and more energy leaks into cladding area. Figure 4.4, Figure 4.5, Figure 4.6 and Figure 4.7 shows how first, second, third and fourth mode profiles affected by changes of radius. The guided modes modes turns to leaky modes with the decrease of radius. When the radius becomes smaller than 25 μm, all guided modes disappear and turn into leaky modes.

It is also noted from Figure 4.2 that the imaginary part of effective indices of higher order
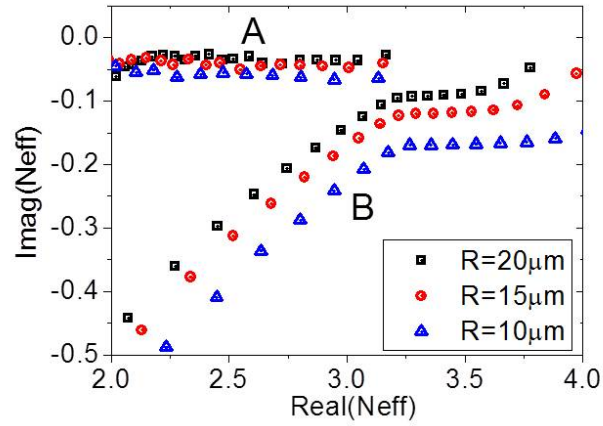
46

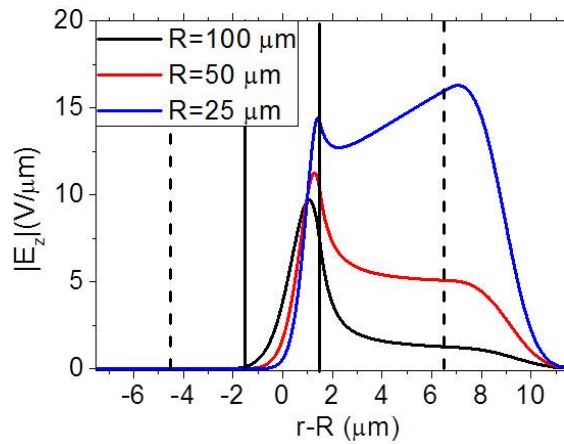Figure 4.3: Effective indices with relatively small bending radius

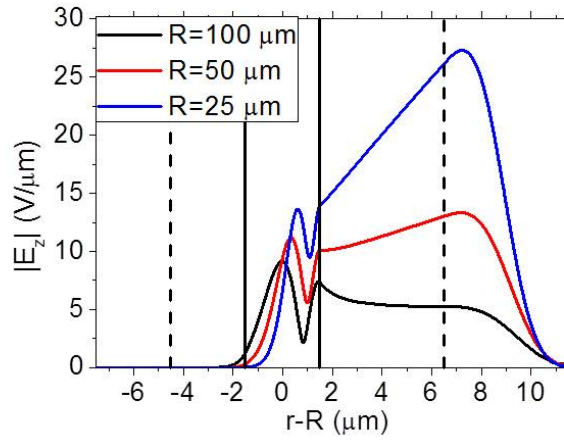Figure 4.4: Profile of first mode

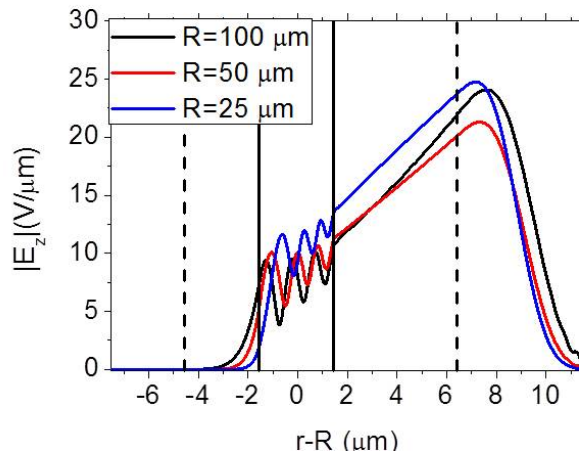Figure 4.5: Profile of second mode
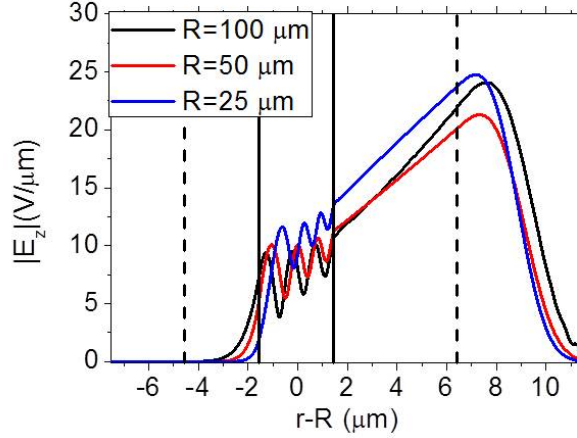

Figure 4.6: Profile of third Mode

Figure 4.7: Profile of fourth mode

modes is relatively large, which means those modes suffers great loss while propagating along z direction. However, those modes are critical in analysis of bending structure since lower order modes are lost in the bending and only higher order modes could propagate along the bending direction. Figure 4.8 shows the excitation of every mode when launching fundamental mode from left side. As it shows, high order modes become more important in contribute energy transfer when radius becomes smaller. Figure 4.2 shows the convergence process of residual error with different radiuses. It shows for smaller radius, the residual error is larger and converges slowly, thus larger number of modes are needed to ensure accurate results.

Figure 4.9 and Figure 4.10 show the transmission of a straight-bend-straight structure when fundamental mode launched from left. For bending structures with radius of 100 μm, only two modes are needed to get accurate results. While for structures with smaller radius, like 25 μm, more modes are needed to consider in the propagation process in order to get accurate results.

49
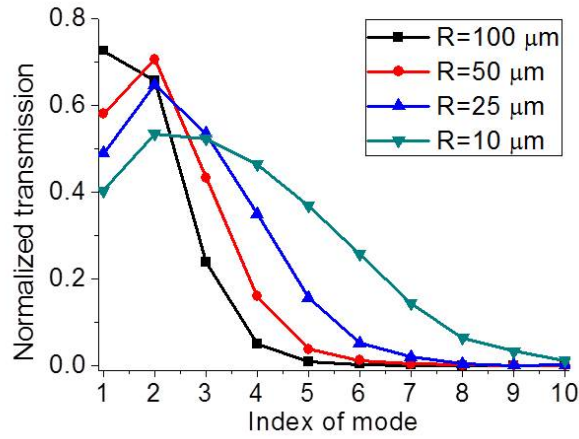
Figure 4.8: Transmission coefficient with fundamental mode lanched
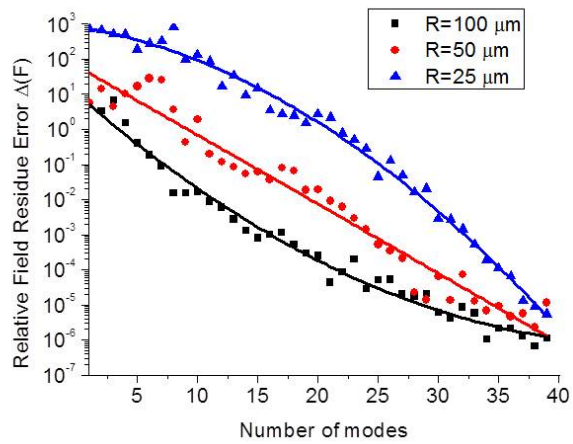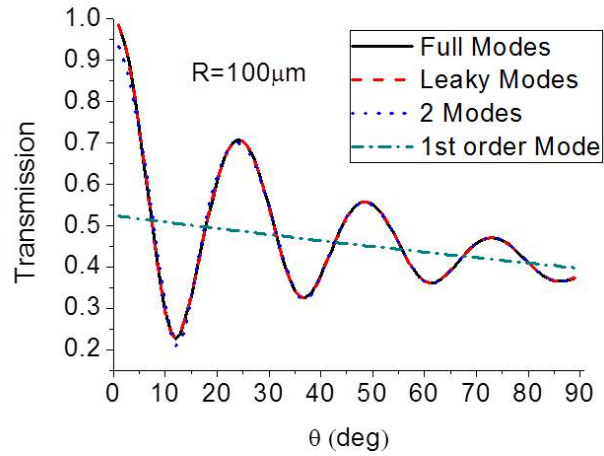
Figure 4.9: Bending transmission when radius is 100 μm
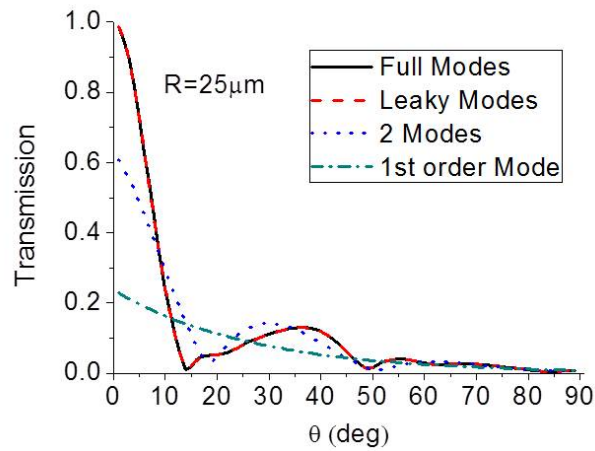
Figure 4.10: Bending transmission when radius is 25 μm

4.3   Summary

In this chapter, the Mode Matching Method are used in the simulation and analysis of bending structures. Firstly, the bending structures are transformed into planar waveguides such that the conventional complex mode solvers could be applied with little modification. Secondly, bending structures with different radiuses are analyzed. The result shows that for bending structures with smaller radiuses, high order modes play import roles in energy transfer while propagating along the bending part. It indicates that more leaky modes needs to be considered to get accurate results especially for bending structures with smaller radiuses.

Chapter 5

Grating Simulation

Another commonly used method in waveguide simulation is Coupled Mode Theory [15]. It is especially suitable for analysis of gratings with weak refractive index perturbation. In this chapter, the Complex Coupled Mode theory is provided and results will be compared with Mode Matching Method.

5.1   Complex Coupled Mode Theroy

Basically the Coupled Mode Theory is a perturbational approach to analyze the vibrational systems. The Coupled Mode Theory states that the modal coefficients satisfy a set of differential equations, known as Coupled Mode Equations. The exact formulas and processes of CMT would be complex, but most of the calculations are usually redundant and thus could be greatly simplified.

5.1.1   Coupled Mode Equations

Assume there is permittivity perturbation within the waveguide and distribution of perturbation along propagation direction could be described by the function

$$\tilde{\epsilon}(x, y, z) = \epsilon(x, y, z) + \Delta\epsilon(x, y, z) \tag{5.1}$$

where the index perturbation $\Delta\epsilon$ is defined as the difference between the index profiles of the practical waveguides under investigation and the reference waveguides for which the complete complex mode set is known.

Suppose that the difference between the perturbed and the reference waveguides is sufficiently small such that we can expand the unknown transverse electromagnetic fields of the perturbed waveguides in terms of the transverse modal fields of the reference waveguides, i.e.

$$
\begin{aligned}
\mathbf{E}_t(x, y, z) &= \sum_n [a_n(z) + b_n(z)] \mathbf{e}_{tn}(x, y) \\
\mathbf{H}_t(x, y, z) &= \sum_n [a_n(z) - b_n(z)] \mathbf{h}_{tn}(x, y) \\
\mathbf{E}_z(x, y, z) &= \sum_n [a_n(z) - b_n(z)] \frac{\epsilon}{\tilde{\epsilon}} \mathbf{e}_{zn}(x, y) \\
\mathbf{H}_z(x, y, z) &= \sum_n [a_n(z) + b_n(z)] \mathbf{h}_{zn}(x, y)
\end{aligned}
\tag{5.2}
$$

where $\mathbf{e}_{tm}(x, y)$, $\mathbf{h}_{tm}(x, y)$, $\mathbf{e}_{zm}(x, y)$ and $\mathbf{h}_{zm}(x, y)$ are the m-th mode's profile distribution for transverse/vertical electrical/magnetic fields, with β_m the propagation constant.

Consider a source $\mathbf{F} = \mathbf{E} \times \mathbf{H}_m - \mathbf{E}_m \times \mathbf{H}$. Here only the m-th forward propagation mode is considered. Applying the Gauss's law to an arbitrary volume of perturbed waveguide from z to $z + \Delta z$ and the transverse section covering all the modal distributed area terminated by PML and PRB

$$\iiint_V \nabla \cdot \mathbf{F} \mathrm{d}v = -\iint_A \mathbf{F}(z) \cdot \hat{z} \mathrm{d}A + \iint_A \mathbf{F}(z+\Delta z) \cdot \hat{z} \mathrm{d}A + \iint_L \mathbf{F} \cdot \hat{\mathbf{n}} \mathrm{d}L \quad (5.3)$$

where A is the transverse section and L is the surface around parallel to the propagation direction. As the PRB applied as boundary, where the field should be zero, the last item at the right hand side shall be zero.

The first item at the left hand side can be further expressed as

$$\iiint_V \nabla \cdot \mathbf{F} \mathrm{d}v = \int_z \iint_A \nabla \cdot \mathbf{F} dA dz \quad (5.4)$$

Substitute into the previous equation and take derivative at both side,

$$\iint_A \nabla \cdot \mathbf{F} \mathrm{d}a = \frac{\partial}{\partial z} \iint_A \mathbf{F} \cdot \hat{z} dA \quad (5.5)$$

The integrand of the left hand side can be simplified as

$$\nabla \cdot \mathbf{F} = \nabla \cdot \mathbf{E} \times \mathbf{H}_m - \nabla \cdot \mathbf{E}_m \times \mathbf{H}$$

$$= (\nabla \times \mathbf{E}) \cdot \mathbf{H}_m - \mathbf{E} \cdot (\nabla \times \mathbf{H}_m) - (\nabla \times \mathbf{E}_m) \cdot \mathbf{H} + \mathbf{E}_m \cdot (\nabla \times \mathbf{H})$$

$$= -j\omega\mu_0 \mathbf{H} \cdot \mathbf{H}_m - \mathbf{E} \cdot j\omega\epsilon \mathbf{E}_m + j\omega\mu_0 \mathbf{H}_m \cdot \mathbf{H} + \mathbf{E}_m \cdot j\omega\tilde{\epsilon}\mathbf{E}$$

$$= j\omega(\tilde{\epsilon} - \epsilon)\mathbf{E} \cdot \mathbf{E}_m$$

$$= j\omega(\tilde{\epsilon} - \epsilon)(\mathbf{E}_t \cdot \mathbf{e}_t + \mathbf{E}_z \cdot \mathbf{e}_z) \exp(-j\beta_m z) \tag{5.6}$$

$$= j\omega(\tilde{\epsilon} - \epsilon) \sum_n \left[(a_n + b_n)\mathbf{e}_{tn} \cdot \mathbf{e}_{tm} + \frac{\epsilon}{\tilde{\epsilon}}(a_n - b_n)\mathbf{e}_{zn} \cdot \mathbf{e}_{zm} \right] \exp(-j\beta_m z)$$

$$= j\omega\epsilon_0(\tilde{n}^2 - n^2) \Big[\sum_n (\mathbf{e}_{tn} \cdot \mathbf{e}_{tm} + \frac{n^2}{\tilde{n}^2})a_n$$

$$+ \sum_n (\mathbf{e}_{tn} \cdot \mathbf{e}_{tm} - \frac{n^2}{\tilde{n}^2}\mathbf{e}_{zn} \cdot \mathbf{e}_{zm})b_n \Big] \exp(-j\beta_m z)$$

Define the forward and backward coupling coefficients

$$\kappa_{mn} = \frac{\omega\epsilon_0}{4} \int \int_A (\tilde{n}^2 - n^2)(\mathbf{e}_{tn} \cdot \mathbf{e}_{tm} - \frac{n^2}{\tilde{n}^2}\mathbf{e}_{zn} \cdot \mathbf{e}_{zm})\mathrm{d}A$$
$$\chi_{mn} = \frac{\omega\epsilon_0}{4} \int \int_A (\tilde{n}^2 - n^2)(\mathbf{e}_{tn} \cdot \mathbf{e}_{tm} + \frac{n^2}{\tilde{n}^2}\mathbf{e}_{zn} \cdot \mathbf{e}_{tm})\mathrm{d}A \tag{5.7}$$

Then the left hand side will be simplified as

$$\int \int_A \nabla \cdot \mathbf{F} dA = 4j(\sum_n \kappa_m n a_n + \sum_n \chi_{mn} b_n) \exp(-j\beta_m z) \tag{5.8}$$

For the integrand of the right hand side, do the same substitution to simplify it

$$
\begin{aligned}
\mathbf{F} \cdot \hat{z} &= (\mathbf{E} \times \mathbf{H}_m - \mathbf{E}_m \times \mathbf{H}) \cdot \hat{z} \\
&= (\mathbf{E}_t \times \mathbf{H}_{tm} - \mathbf{E}_{tm} \times \mathbf{H}_t) \cdot \hat{z} \\
&= \sum_n [(a_n + b_n)\mathbf{e}_{tn} \times \mathbf{h}_{tm} \cdot \hat{z} - (a_n - b_n)\mathbf{e}_{tm} \times \mathbf{h}_{tn} \cdot \hat{z}] \exp(-j\beta_m z) \\
&= 2 \sum_n b_n \mathbf{e}_{tn} \times \mathbf{h}_{tm} \cdot \hat{z} \exp(-j\beta_m z)
\end{aligned}
\tag{5.9}
$$

Consider the complex modes' orthogonality and normalization,

$$
\iint_A \mathbf{e}_{tm} \times \mathbf{h}_{tn} \cdot \hat{z}\,\mathrm{d}A = 2N_m \delta_{mn}
\tag{5.10}
$$

where δ_{mn} is the Kronecker's delta. Thus the right hand side could be rewritten as

$$
\begin{aligned}
\frac{\partial}{\partial} \iint_A \mathbf{F} \cdot \hat{z}\,\mathrm{d}A &= 4N_m \frac{\partial}{\partial z} b_m \exp(-j\beta_m z) \\
&= 4N_m (-j\beta_m b_m + \frac{\partial b_m}{\partial z}) \exp(-j\beta_m z)
\end{aligned}
\tag{5.11}
$$

So the coupling equation for the m-th backward propagation mode is obtained as

$$
N_m(\frac{\partial b_m}{\partial z} - j\beta_m b_m) = j \sum_n \chi_{mn} a_n + j \sum_n \kappa_{mn} b_n
\tag{5.12}
$$

Similarly, consider source as $\mathbf{F} = \mathbf{E} \times \mathbf{H}_{-m} - \mathbf{E}_{-m} \times \mathbf{H}$. Follow the same procedure, the other coupling equation is

$$N_m(\frac{\partial a_m}{\partial z} + j\beta_m a_m) = -j\sum_n \kappa_{mn} a_n - j\sum_n \chi_{mn} b_n \tag{5.13}$$

5.1.2   Simplified Coupled Mode Equations

The general form of the Complex Coupled Mode Equations are

$$
\begin{aligned}
N_m\big(\frac{\partial a_m}{\partial z} + j\beta_m a_m\big) &= -j\sum_n \kappa_{mn} a_n - j\sum_n \chi_{mn} b_n \\
N_m\big(\frac{\partial b_m}{\partial z} - j\beta_m b_m\big) &= j\sum_n \kappa_{mn} b_n + j\sum_n \chi_{mn} a_n
\end{aligned}
\tag{5.14}
$$

which is a matrix of $N \times N$ differential equations. In practice, usually the coupling between a few specific modes is significant, thus most of the equations could be reduced. In the case of gratings, due to the periodic nature, the equations could be simplified further.

To extract envelop from the fast varying components, let

$$
\begin{aligned}
a_n &= A_n \exp(-j\beta_n z) \\
b_n &= B_n \exp(+j\beta_n z)
\end{aligned}
\tag{5.15}
$$

The coupling equations shall be rewritten with A_n and B_n as

$$N_m\frac{\partial A_m}{\partial z} = -j\sum_n \kappa_{mn} A_n \exp[-j(\beta_n - \beta_m)z] - j\sum_n \chi_{mn} B_n \exp[j(\kappa_n + \kappa_m)z] \tag{5.16}$$

In the case of grating, the refractive indices of the core layer are modulated according to a period function, which lead to the period changes of the coupling coefficients.

$$
\kappa_{mn} = \sum_{l=-\infty}^{+\infty} D_{mn}^l \exp(jl\frac{2\pi}{\Lambda}z)
$$
$$
\chi_{mn} = \sum_{l=-\infty}^{+\infty} C_{mn}^l \exp(jl\frac{2\pi}{\Lambda}z)
$$

(5.17)

where Λ is the period of the grating.

Then the coupling equations could be written as

$$
N_m \frac{\partial A_m}{\partial z} = -j \sum_n A_n \sum_l D_{mn}^l \exp[-j(\beta_n - \beta_m - l\frac{2\pi}{\Lambda})z]
$$

(5.18)

Firstly, consider only the largest Fourier expansion terms, that is, $l = -1, 0, 1$, or the 1st-order grating effect and ignore all other higher-order harmonics. Secondly, ignore the coupling among cladding modes, including cladding-mode self-scattering. Thirdly, the usual synchronous approximation is employed. We neglect all driving terms on the right hand sides that oscillate too rapidly to contribute significantly to the change of the mode amplitudes on the left hand sides and keep only those terms that either do not oscillate at all or oscillate at a very small rate. Then the coupling equations between the fundamental mode and the cladding modes are simplified to

$$N_1 \frac{\partial A_1}{\partial z} = -jA_1 D_{11}^0 - \sum_n jA_n D_{1n}^{-1} \exp[j(\beta_1 - \beta_n - \frac{2\pi}{\Lambda})z]$$

$$N_n \frac{\partial A_n}{\partial z} = -jA_1 D_{n1}^1 \exp[-j(\beta_1 - \beta_n - \frac{2\pi}{\Lambda})z]$$

(5.19)

which describes co-propagating interactions in a long-period grating.

Let

$$A_1 = \tilde{A}_1 \exp(-j\frac{D_{11}^0}{N_1})$$

(5.20)

Substitute A_1 with $\tilde{A}_1$ and rewrite $\tilde{A}_1$ as A_1, finally the simplified complex coupled mode equations are obtained as

$$N_1 \frac{\partial A_1}{\partial z} = \sum_n -jA_n D_{1n}^{-1} \exp[j(\beta_1 - \beta_n - \frac{2\pi}{\Lambda} + \frac{D_{11}^0}{N_1}]$$

$$N_n \frac{\partial A_n}{\partial n} = -jA_1 D_{n1}^1 \exp[-j(\beta_1 - \beta_n - \frac{2\pi}{\Lambda} + \frac{D_{11}^0}{N_1}]$$

(5.21)

In a over-simplified situation that only one mode interacts with fundamental mode significantly and other couplings are neglected, this specific mode satisfies

$$\beta_1 - \beta_n - \frac{2\pi}{\Lambda} = 0$$

(5.22)

which is also known as the Bragg condition.

Similar equations could be obtained for contra-propagating gratings.

Parameter	Value
core refractive index	1.458
core thickness	5.25 μm
cladding refractive index	1.45
cladding thickness	59.875 μm
air thickness	10 μm
grating index perturbation Δn	1×10^{-4}
grating period	$269.4145 \times 10^{-6} \mu m$
grating length	25 mm
working wavelength λ	1.85 μm
PML thickness d_{PML}	50 μm
PML reflection coefficient R_{PML}	10^{-2}

Table 5.1: Parameters used in simulation of long-period grating

5.2   Grating Simulation using Coupled Mode Theory

5.2.1   Long-Period Grating

Consider a long-period grating shown in Figure 5.1. The parameters used in simulation is shown in Table 5.1 [16].

Figure 5.2 shows the coupling coefficients of fundamental mode with every other modes. Large coupling coefficients means strong interaction and significant energy transfer with fundamental mode. The first peak appears at 21, indicating the 21-th mode plays most significant role in coupling and the refractive index 21-th mode satisfy the Bragg condition.
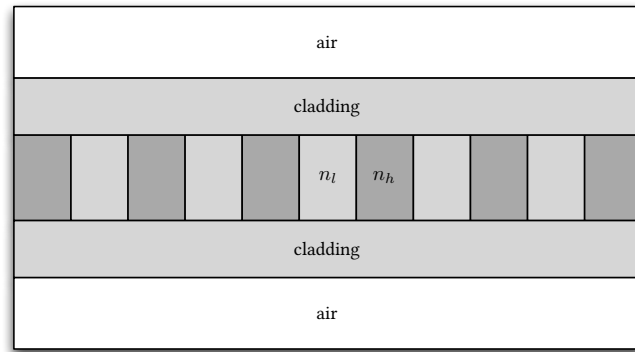
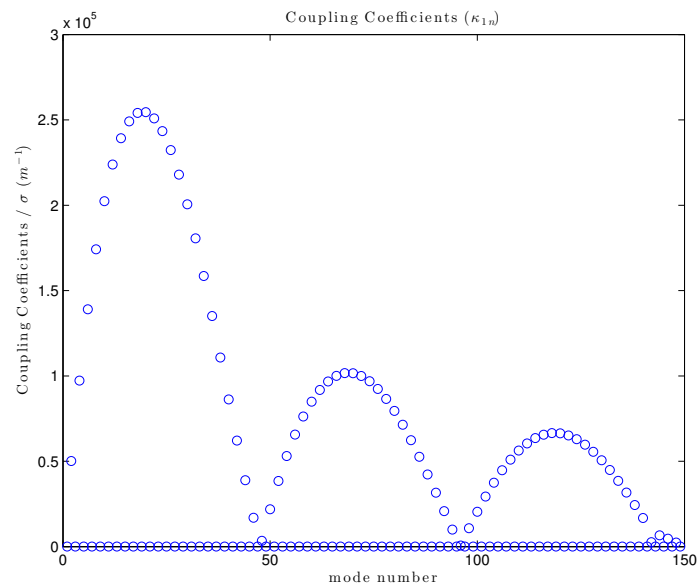Figure 5.1: Long-period grating
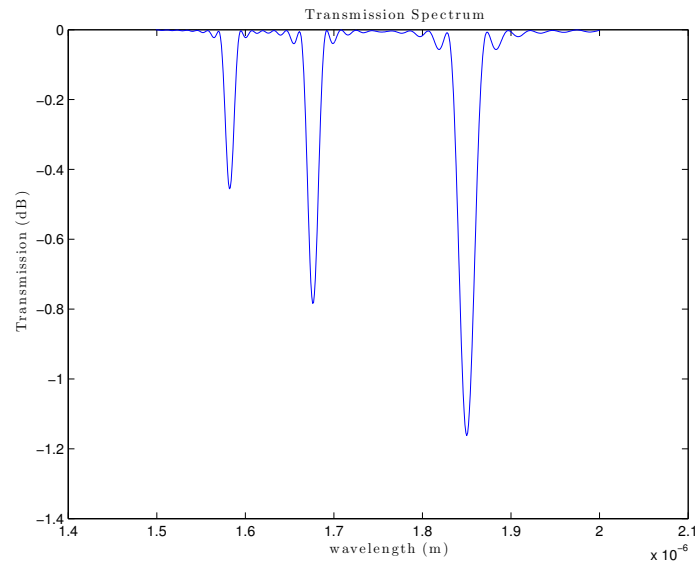

Figure 5.2: Coupling Coefficients

Figure 5.3: Transmission spectrum

The transmission spectrum in Figure 5.3 verifies the statement. The other two smaller peaks in spectrum corresponding to the other two peaks in coupling coefficients.

5.2.2 Long-Period Grating with Deposited Region

Figure 5.4 shows a long-period grating with deposited region. The parameters of the structure is listed in Table 5.2.

The refractive index of overlay layers is larger than even core refractive index, thus more energy will be concentrated within the overlay layers, thus made the structure highly depend on the overlay parameters. Figure 5.5 and Figure 5.6 show how the effective indices affected by the overlay thickness. The effective indices shift to the lower order mode's value with the increase of overlay thickness.

Parameter	Value
core refractive index	1.47
core thickness	8.3 μm
cladding refractive index	1.4647
cladding thickness	58.35 μm
overlay refractive index	1.62 + 0.004i
overlay thickness	0.23
air thickness	10 μm
grating index perturbation Δn	2.85×10^{-4}
grating period	$245.36 \times 10^{-6} \mu m$
grating length	20 mm
working wavelength λ	1.2 μm
PML thickness d_{PML}	50 μm
PML reflection coefficient R_{PML}	10^{-2}

Table 5.2: Parameters used in simulation of grating with deposited region
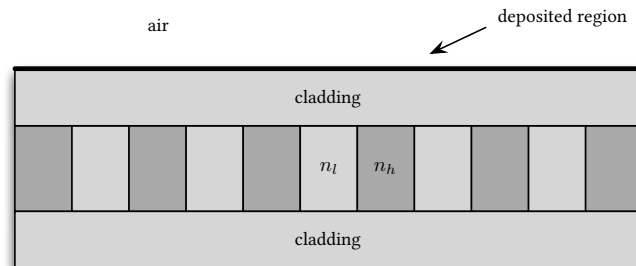

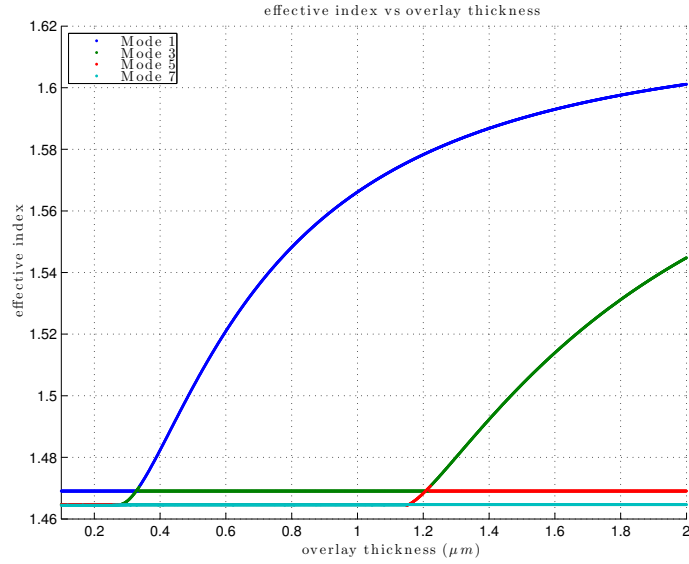Figure 5.4: Long-period grating with a deposited region

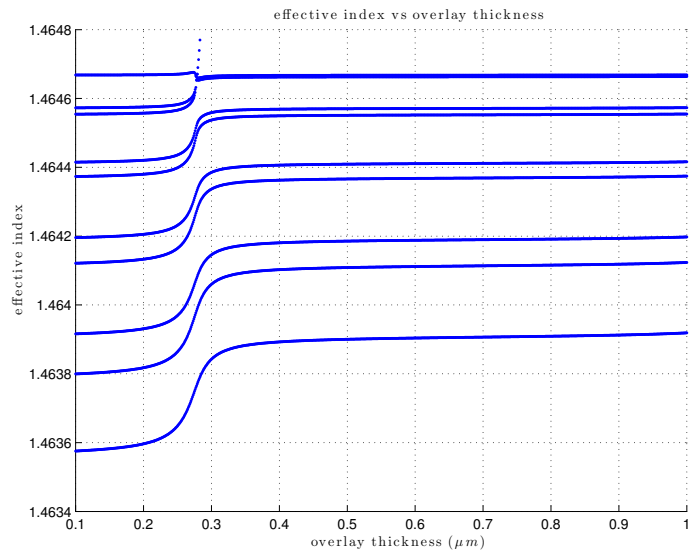Figure 5.5: Effective indices vs overlay thickenss

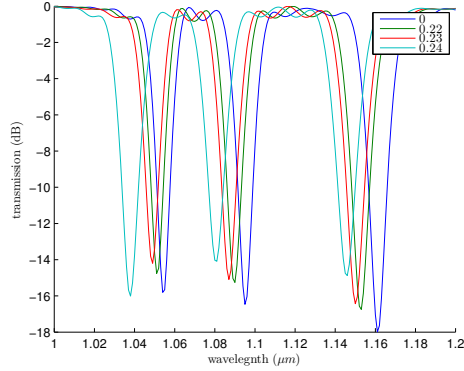Figure 5.6: Effective indices vs overlay thickness

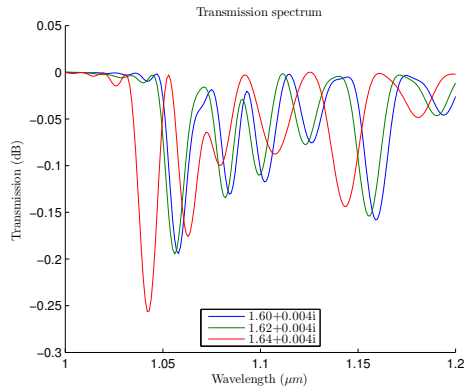Figure 5.7: Transmission spectrum vs overlay thickness

Figure 5.8: Transmission spectrum vs overlay refractive index

Figure 5.7 shows the transmission spectrum with different overlay thicknesses, and Figure 5.8 shows the spectrum with different overlay refractive indices. It is clear that small changes of parameters of the overlay layer will greatly changes the transmission spectrum of the grating.

5.3 Grating Simulation using Mode Matching Method

Mode Matching Method could be used in grating simulations as well. The overall transfer matrix or scatter matrix could be obtained by cascade individual matrix. Since gratings are periodic structures, the algorithm of reduction could be used to accelerate computation and reduce numerical truncation error.

More over, the Mode Matching Method has a few advantages over Coupled Mode Theory. Firstly, the CMT can only generate accurate results for gratings with weak index corrugation. While MMM also lost precision for strong index perturbation, it usually provides better numerical results. Secondly, MMM could be used to analyze higher order gratings without modifications. In this section, MMM will be applied to simulate a typical long-period grating, a second-order grating and a strong index corrugation grating.

5.3.1 Long-Period Grating

Figure 5.9 shows a typical long-period grating. The parameters used in simulation are listed below
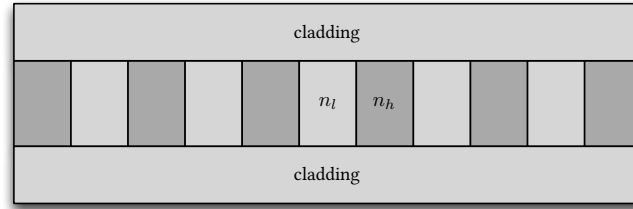
Figure 5.9: Typical long-period graing

Parameter	Value
core refractive index n_{co}	1.458
core thickness d_{co}	5 μm
cladding refractive index n_{cl}	1.45
cladding thickness d_{cl}	5 μm
working wavelength λ	1.55 μm
PML thickness d_{PML}	10 μm
PML reflection coefficient R_{PML}	10^{-5}
grating index perturbation Δn	0.001
grating duty cycle	0.5
grating period Λ	0.5326 μm
grating number of periods	2^{10}

The reflection and transmission grating of the grating is shown in Figure 5.10. The results are similar to Coupled Mode Theory.

The spectrum of second-order grating could be could also be easily obtained by changing grating period Λ to $1.0652\mu m$ and grating number of periods to 2^{15}. The results is shown in Figure 5.11.
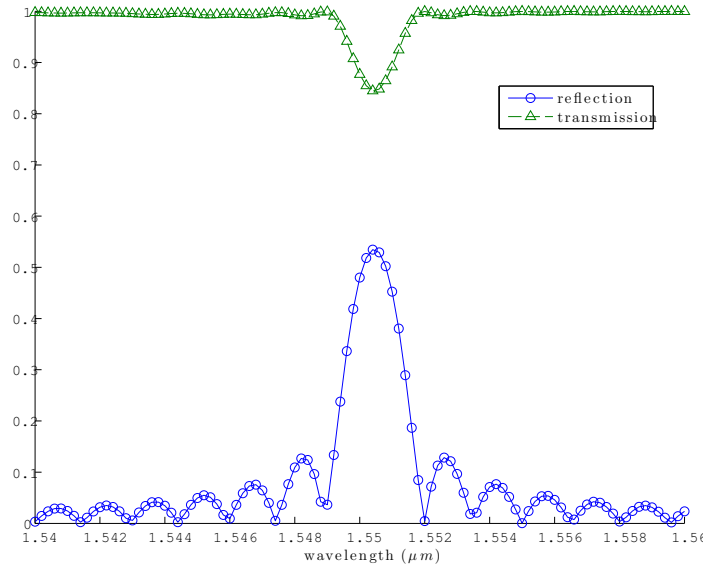
Figure 5.10: Reflection and transmission spectrum of first-order grating
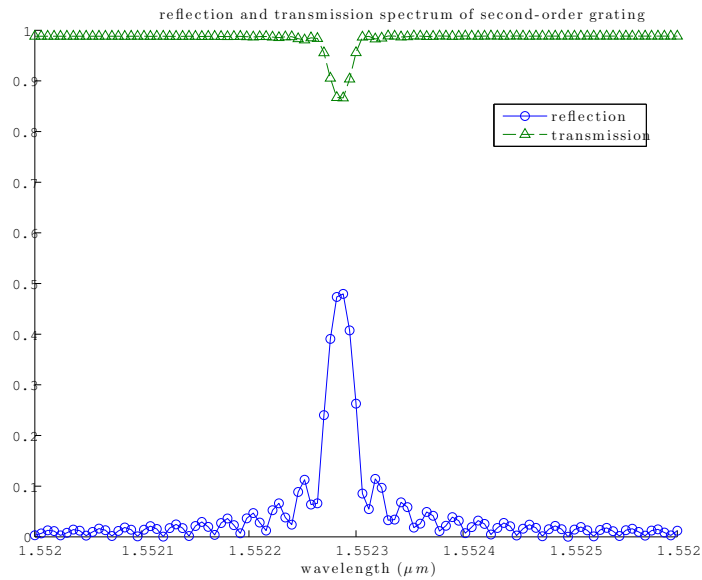
Figure 5.11: Reflection and transmission spectrum of first-order grating

Figure 5.12: Grating with strong corrugation
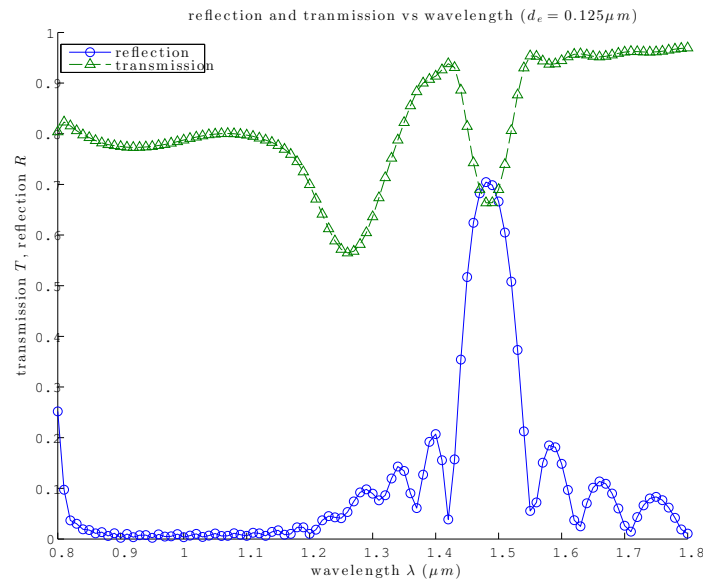
Figure 5.13: Reflection and transmission spectrum of a strong corrugation grating

5.3.2   Long-Period Grating with Strong Corrugation

Figure 5.12 shows a grating with strong index corrugation and small number of periods. Figure 5.3 lists of parameters used in the simulation [20],

Figure 5.13 shows the reflection and transmission spectrum of the grating.

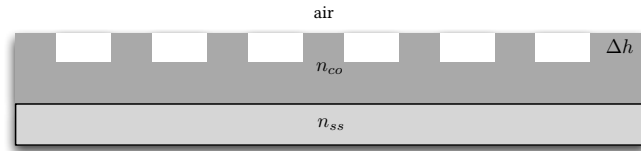| Parameter	Value
core refractive index n_{co}	1.97916
core thickness d_{co}	0.5 μm
air thickness d_{air}	3 μm
substrate refractive index n_{ss}	1.44409
substrate thickness	3 μm
working wavelength λ	1.48 μm
PML thickness d_{PML}	9 μm
PML reflection coefficient R_{PML}	10^{-4}
grating corrugate depth Δh	0.125
grating duty cycle	0.5
grating period Λ	0.43 μm
grating number of periods	20

Table 5.3: Parameters used in simulation of grating with strong corrugation

5.4   Summary

In this chapter, the Coupled Mode Equations are derived and explained. In the case of gratings, simplified equations are obtained. Comparison and discussion are made between Coupled Mode Theory and Mode Matching Method. Several typical gratings are simulated and analyzed using both methods.

Chapter 6

Conclusion

This thesis covers various topics of waveguide simulation using Mode Matching Method as well as Coupled Mode Theory. The Finite-Difference Method based mode solvers are presented and higher order difference schemes are briefly touched. Pros and Cons of the method are discussed. The Finite-Difference based complex mode solvers are then improved with regarding to asymmetric structures by method of Weighted Optical Path Distance. Numerical results shows that the technique will reduce fluctuation mode matching process. Conventional Complex Mode Matching Method is presented and the matching formulas are improved though matrix optimization. The simulation process proved that the IMMM will accelerate convergence process and provides more accurate results. Then several typical waveguide structures are investigated and analyzed, including bending structures, straight-bending-straight structures, long-period gratings, gratings with deposited layers and gratings with strong index corrugations. It is concluded that the above optimization could help reduce fluctuations and speed up convergence of the mode

matching process. It is also concluded that high order complex modes play crucial roles in the process of energy transfer within waveguides that have strong radiation effects.

As the time is limited, the topics are not fully covered and many more interesting issues are yet to be investigated. Of which the comparison of results from MMM and CMT could be made and discussed. Also intriguing is analysis of out-of-plane losses in structures with prominent radiation effect, as well as analysis and discussion of higher-order grating structures.

Bibliography

[1] Jean-Pierre Berenger. A perfectly matched layer for the absorption of electromagnetic waves. *Journal of computational physics*, 114(2):185–200, 1994.

[2] Stephen D Gedney. An anisotropic perfectly matched layer-absorbing medium for the truncation of fdtd lattices. *Antennas and Propagation, IEEE Transactions on*, 44(12):1630–1639, 1996.

[3] MS Stern et al. Finite difference analysis of planar optical waveguides. *Progress In Electromagnetics Research*, 10:123–186, 1995.

[4] Jianwei Mu and Wei-Ping Huang. Simulation of three-dimensional waveguide discontinuities by a full-vector mode-matching method based on finite-difference schemes. *Optics express*, 16(22):18152–18163, 2008.

[5] MS Stern. Semivectorial polarised finite difference method for optical waveguides with arbitrary index profiles. In *Optoelectronics, IEE Proceedings J*, volume 135, pages 56–63. IET, 1988.

[6] C Vassallo. Improvement of finite difference methods for step-index optical waveguides. *IEE Proceedings J (Optoelectronics)*, 139(2):137–142, 1992.

[7] Yih-Peng Chiou, Yen-Chung Chiang, and Hung-Chun Chang. Improved three-point formulas considering the interface conditions in the finite-difference analysis of step-index optical devices. *Journal of lightwave technology*, 18(2):243, 2000.

[8] Yih-Peng Chiou and Cheng-Han Du. Arbitrary-order interface conditions for slab structures and their applications in waveguide analysis. *Optics express*, 18(5):4088–4102, 2010.

[9] Haibo Liang, Jianwei Mu, Xun Li, and Wei-Ping Huang. Insights into complex berenger modes: a view from the weighted optical path distance perspective. *Optics letters*, 39(9):2811–2814, 2014.

[10] Jianxin Zhu and Ya Yan Lu. Asymptotic solutions of eigenmodes in slab waveguides terminated by perfectly matched layers. *JOSA A*, 30(10):2090–2095, 2013.

[11] George V Eleftheriades, AS Omar, LPB Katehi, and Gabriel M Rebeiz. Some important properties of waveguide junction generalized scattering matrices in the context of the mode matching technique. *Microwave Theory and Techniques, IEEE Transactions on*, 42(10):1896–1903, 1994.

[12] Gene H Golub and Charles F Van Loan. *Matrix computations*, volume 3. JHU Press, 2012.

[13] Haibo Liang, Jianwei Mu, Xun Li, and Weiping Huang. Improved complex mode matching method for optical waveguides analysis. In *Integrated Photonics Research, Silicon and Nanophotonics*, pages IT1A–5. Optical Society of America, 2014.

[14] Mordehai Heiblum and Jay H Harris. Analysis of curved optical waveguides by conformal transformation. *IEEE Journal of Quantum Electronics*, 11:75–83, 1975.

[15] Wei-Ping Huang and Jianwei Mu. Complex coupled-mode theory for optical waveguides. *Optics express*, 17(21):19134–19152, 2009.

[16] Turan Erdogan. Cladding-mode resonances in short-and long-period fiber grating filters. *JOSA A*, 14(8):1760–1773, 1997.

[17] AMOS Hardy, David F Welch, and William Streifer. Analysis of second-order gratings. *Quantum Electronics, IEEE Journal of*, 25(10):2096–2105, 1989.

[18] Rui Wang, Lin Han, Jianwei Mu, and Weiping Huang. Simulation of waveguide crossings and corners with complex mode-matching method. *Journal of Lightwave Technology*, 30(12):1795–1801, 2012.

[19] Kenneth O Hill and Gerald Meltz. Fiber bragg grating technology fundamentals and overview. *Journal of lightwave technology*, 15(8):1263–1276, 1997.

[20] J Čtyrokỳ, S Helfert, R Pregla, Peter Bienstman, Roel Baets, R De Ridder, R Stoffer, G Klaasse, J Petráček, Ph Lalanne, et al. Bragg waveguide grating as a 1d photonic band gap structure: Cost 268 modelling task. *Optical and Quantum Electronics*, 34(5):455–470, 2002.

[21] Fdtd solutions from lumerical solutions, inc.

[22] Peter Bienstman and Roel Baets. Optical modelling of photonic crystals and vcsels using eigenmode expansion and perfectly matched layers. *Optical and Quantum Electronics*, 33(4-5):327–341, 2001.

[23] Henk Derudder, Frank Olyslager, Daniel De Zutter, and Steve Van den Berghe.

Efficient mode-matching analysis of discontinuities in finite planar substrates using perfectly matched layers. *Antennas and Propagation, IEEE Transactions on*, 49(2):185–195, 2001.

[24] SL Lin, LW Li, TS Yeo, and MS Leong. Novel unified mode matching analysis of concentric waveguide junctions. *IEE Proceedings-Microwaves, Antennas and Propagation*, 148(6):369–374, 2001.

[25] George V Eleftheriades, AS Omar, LPB Katehi, and Gabriel M Rebeiz. Some important properties of waveguide junction generalized scattering matrices in the context of the mode matching technique. *Microwave Theory and Techniques, IEEE Transactions on*, 42(10):1896–1903, 1994.

[26] ZOU Chang-Ling, SHU Fang-Jie, SUN Fang-Wen, GONG Zhao-Jun, HAN Zheng-Fu, and GUO Guang-Can. Theory of free space coupling to high-q whispering gallery modes. 2014.

[27] Donghwan Ahn, Ching-yin Hong, Jifeng Liu, Wojciech Giziewicz, Mark Beals, Lionel C Kimerling, Jurgen Michel, Jian Chen, and Franz X Kńrtner. High performance, waveguide integrated ge photodetectors. *Optics Express*, 15(7):3916–3921, 2007.

[28] Tsung-Yang Liow, Kah-Wee Ang, Qing Fang, Jun-Feng Song, Yong-Zhong Xiong, Ming-Bin Yu, Guo-Qiang Lo, and Dim-Lee Kwong. Silicon modulators and germanium photodetectors on soi: monolithic integration, compatibility, and performance optimization. *Selected Topics in Quantum Electronics, IEEE Journal of*, 16(1):307–315, 2010.

[29] WC Chew, JM Jin, and E Michielssen. Complex coordinate stretching as a generalized absorbing boundary condition. *Microwave and Optical Technology Letters*, 15(6):363–369, 1997.

[30] Andrea Melloni, Paolo Monguzzi, Raffaella Costa, and Mario Martinelli. Design of curved waveguides: the matched bend. *JOSA A*, 20(1):130–137, 2003.

[31] Wangqing Yuan and Douglas C Hall. A general scaling rule for matched bend waveguides. *Lightwave Technology, Journal of*, 29(24):3786–3796, 2011.

[32] KR Hiremath, M Hammer, R Stoffer, L Prkna, and J Čtyrokỳ. Analytic approach to dielectric optical bent slab waveguides. *Optical and Quantum Electronics*, 37(1-3):37–61, 2005.

[33] Peter Bienstman, E Six, M Roelens, Mathias Vanwolleghem, and Roel Baets. Calculation of bending losses in dielectric waveguides using eigenmode expansion and perfectly matched layers. *Photonics Technology Letters, IEEE*, 14(2):164–166, 2002.

[34] Weng Cho Chew and William H Weedon. A 3d perfectly matched medium from modified maxwell's equations with stretched coordinates. *Microwave and optical technology letters*, 7(13):599–604, 1994.